CHAPTER 5. RESULTS

5.1 Density

Table 5-1 displays the density values of *SLS* PA-12 at 0° and 90° orientations and of *IM* PA-12. The density of *IM* PA-12 is higher than that of *SLS* PA-12, with no differences between 0° and 90° orientations.

These results are lower than the density of neat PA-12, which is 1.02 g/cm^3 [137]. Nevertheless, the *IM* PA-12 material is almost full dense, with only a porosity percentage of 0.19% versus 3.7% and 3.4% for *SLS* PA-12 at 0° and 90° orientations, respectively. In addition, it is also higher than the theoretical sintered density value of 0.93 g/cm^3 provided by the manufacturer [28] (*Table 4.3*).

5.2 Surface roughness

Table 5-2 shows the surface roughness results for the three materials. While there is no difference in both R_a and R_z parameters between *SLS* orientations, a clear difference is distinguished between *SLS* and *IM* materials.

The roughness average, R_a, of SLS PA-12 are more than one order of magnitude larger than that of *IM* PA-12 and lightly smaller than the values obtained by Guo

Table 5-1. Density measurements obtained with the Archimedes method for IM PA-12 and SLS PA-12 at 0 ° and 90 ° orientations.

Sample ID	Density (g/cm^3)		
	SLS		IM
	0° orientation	90° orientation	
1	0.984	0.991	1.018
2	0.975	0.986	1.018
3	0.982	0.984	1.017
4	0.986	0.979	1.017
Average	**0.982 ± 0.005**	**0.985 ± 0.005**	**1.018 ± 0.005**
Porosity (%)	**3.7 ± 0.5**	**3.4 ± 0.5**	**0.19 ± 0.5**

Table 5-2. Roughness average, Ra, and the average maximum height of the profile, Rz, of SLS PA-12 at 0° and at 90° orientations and of IM PA-12.

	Roughness average, Ra (µm)	Average Maximum height, Rz (µm)
SLS 0° orientation	12 ± 1	69 ± 8
SLS 90° orientation	12 ± 4	60 ± 20
IM	0.4 ± 0.2	3 ± 2

et al. [160] and Xu et al. [161]. In case of the average maximum height of the profile, R_z, the values of *SLS* PA-12 are 20 times higher than those of *IM* PA-12.

5.3 Microstructural analysis

Figure 5-1 shows the characteristic microstructure of the specimens analysed: *SLS at* 0° (*Figure 5-1.a*) and at 90°orientations *(Figure 5-1.b*) and *IM* PA-12 *(Figure 5-1.c*). These images show the spherulites of the crystalline phase, which are usually distributed as spherical crystal colonies with a typical Maltese-Cross pattern, resulting from the birrefrigence of highly ordered lamellae within the spherulites oriented randomly [141], [162]. The spherulites that were fully discernible correspond to those cut in half during the slicing process with the microtome.

Figure 5-2 represents the diameter distribution versus the occurrence probability. The probability density was calculated using a normal distribution as the Kurtosis for all the materials reached values between 0.2 and 0.5, whereas the perfect Gaussian distribution takes values of 0 [163].

Table 5-3 collects the average spherulite diameter, $\overline{D}$, and the standard deviation, *s*, obtained from the measurements. No differences in average size and distribution are observed between *SLS* orientations, obtaining a mean spherulite size around 50 ± 10 µm. This is partly due to the fact that the average size of the spherulites depends upon the cooling conditions and the density of potential nucleating sites for crystallisation, being maintained in the *SLS* process for both orientations.

It is also worth mentioning that the average values of spherulites are quite large and this can be explained by slower crystallisation kinetics during the *SLS* process and a lower nucleation density [142]. The spherulite size of the *IM* PA-12 is much finer, with average size of 13 ± 3 µm, four times lower than

Figure 5-1.Micrographs of SLS PA-12 at 0° orientation (a) and at 90° orientation (b) and of IM PA-12 (c). Dotted lines delineate spherulite contours.

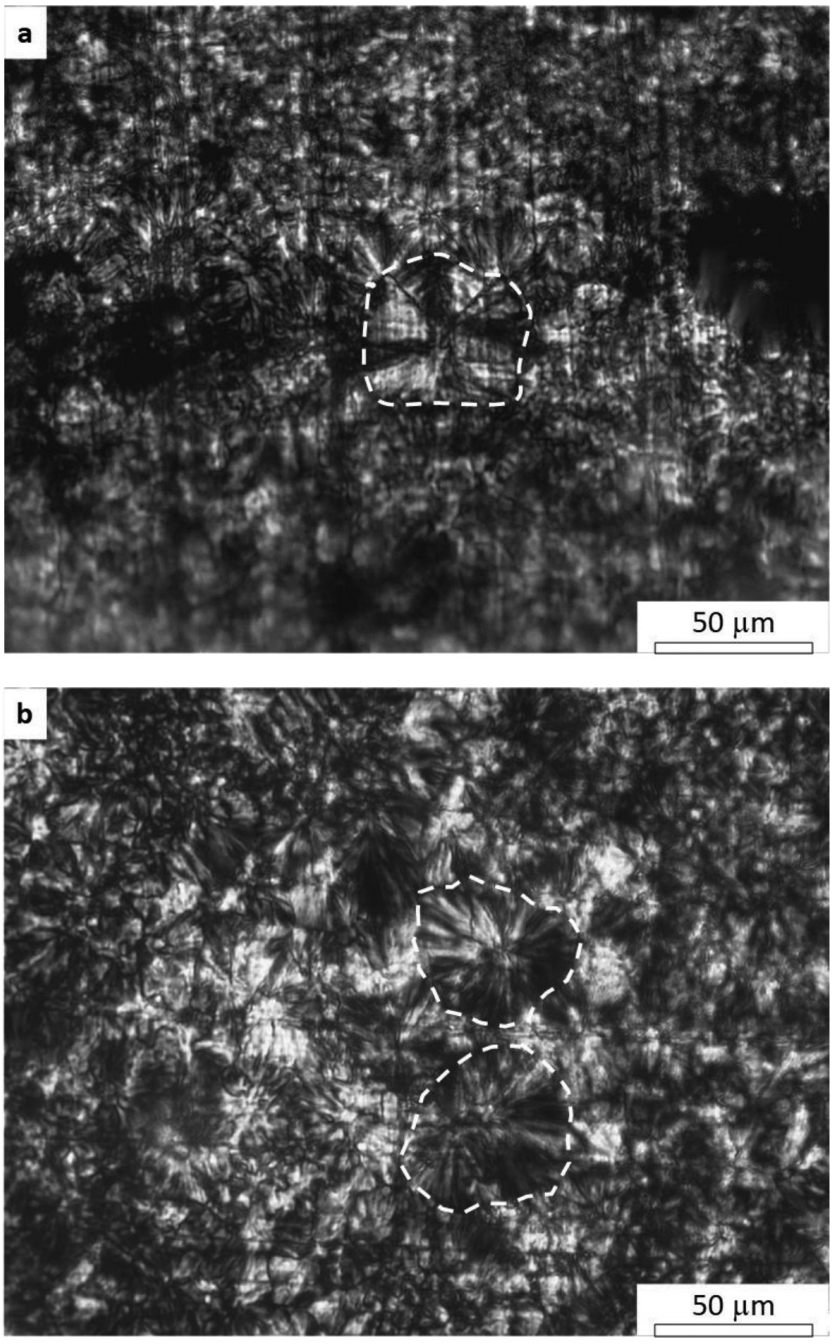

Figure 5-1.Micrographs of SLS PA-12 at 0° orientation (a) and at 90° orientation (b) and of IM PA-12 (c). Dotted lines delineate spherulite contours. (Continued)

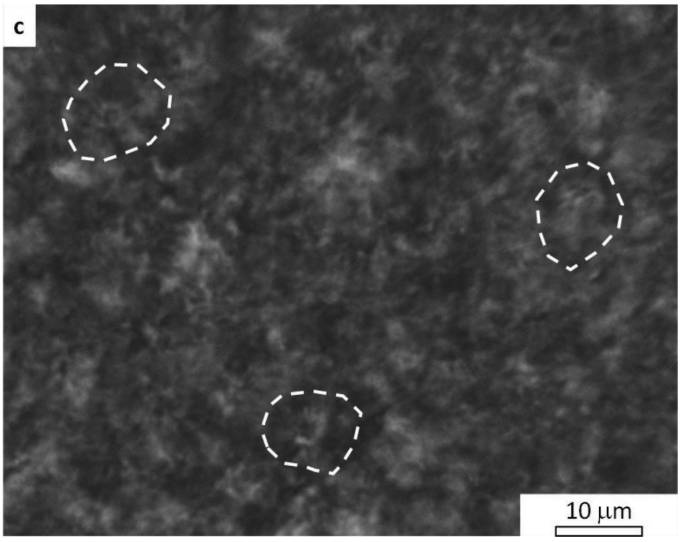

Figure 5-2. Spherulite size distribution for IM PA-12 and SLS PA-12 at 0 ° and 90 ° orientations.

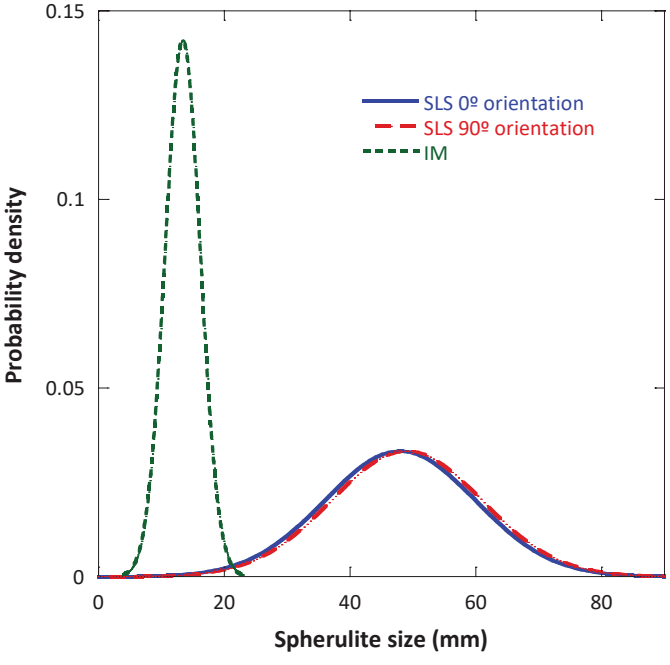

Table 5-3. Normal distribution parameters of the spherulite size of SLS PA-12 at 0 ° and 90 ° orientations and cf IM PA-12: mean spherulitic diameter, $\overline{D}$, and standard deviation, s.

Material	$\overline{D}$ (µm)	s (µm)
SLS 0° orientation	48	12
SLS 90° orientation	49	12
IM	13	3

Figure 5-3. Cross-section of IM-PA12 with a core-skin morphology. The arrows indicate the skin of the material.

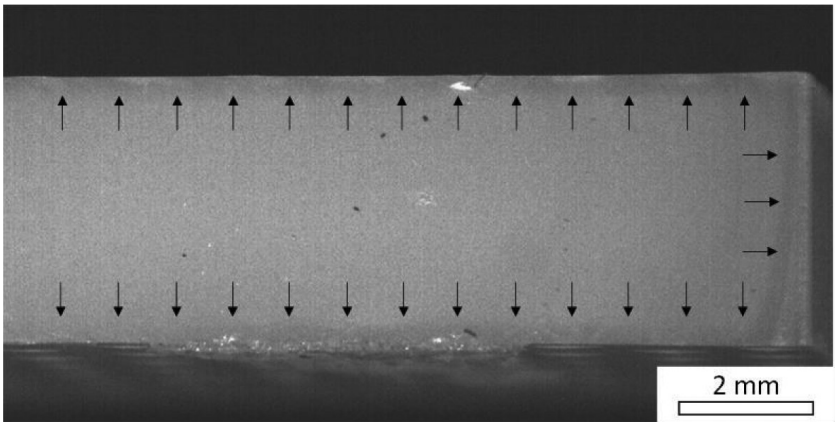

that of *SLS* PA-12. The differences in the spherulite size between the *SLS* and *IM* materials is caused by the thermal history during the manufacturing process. The *IM* material is fully molten before ejection and then cooled rapidly after injection. This rapid cooling allows less crystallisation growth. *SLS* material is also fully molten during laser sintering but the cooling rate is much lower allowing a much-developed transformation of the crystalline structure [164].

Moreover, in case of *IM* PA-12, a skin-core morphology was clearly observable in the cross-sectional samples (*Figure 5-3*), with a skin layer size around 14% of the total sample thickness. The spherulites were measurable in the core as they were not discernible in the surface layer, even with the inspection at the highest magnification of the optical microscope (x1482). The high level of molecular orientation together with the injection speed and the rapid cool-

ing occurring during injection moulding may make difficult the crystallisation process in the skin. However, a micro-spherulitic structure in the core was observable (but always smaller than in *SLS*), due to a different temperature profile in the cooling stage to that undergone in the skin.

5.4 Thermal characterisation

The Differential Scanning Calorimetry (*DSC*) tests performed allow to obtain the thermograms shown in *Figure 5-4*. The crystallinity characteristics, the crystallization temperature, T_c, the melting temperature, T_m, and when observable, the glass transition temperature, T_g, can be computed from them and are collected in *Table 5-4*.

Figure 5-4: Thermographs obtained from DSC tests of SLS-PA 12 (a) at 0° orientation, (b) at 90° orientation and of (c) IM PA-12. The light red line represents the first heating of the test, the blue line shows the cooling process and the dark red line the second heating.

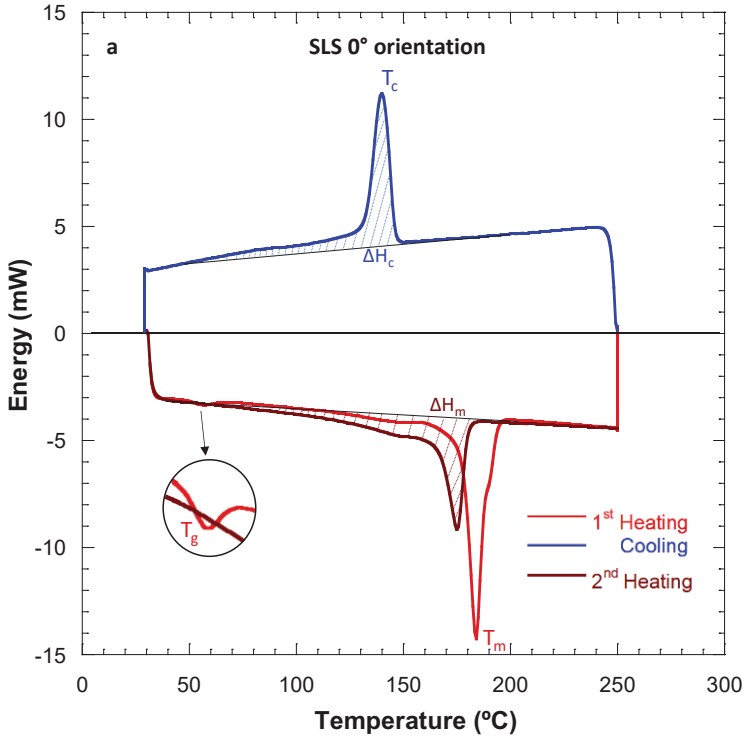

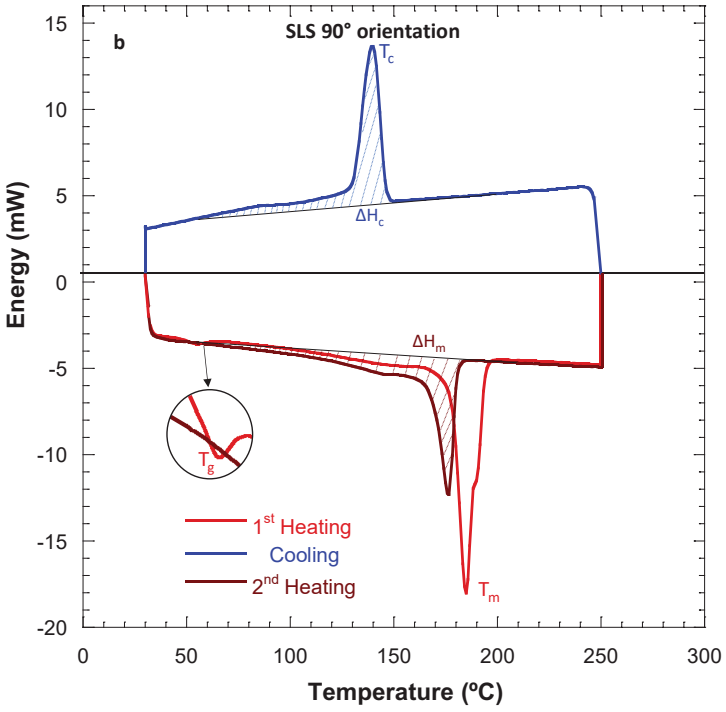
b
SLS 90° orientation
T_c
ΔH_c
ΔH_m
T_g
T_m
1st Heating
Cooling
2nd Heating
Energy (mW)
Temperature (ºC)
15
10
5
0
-5
-10
-15
-20
0
50
100
150
200
250
300

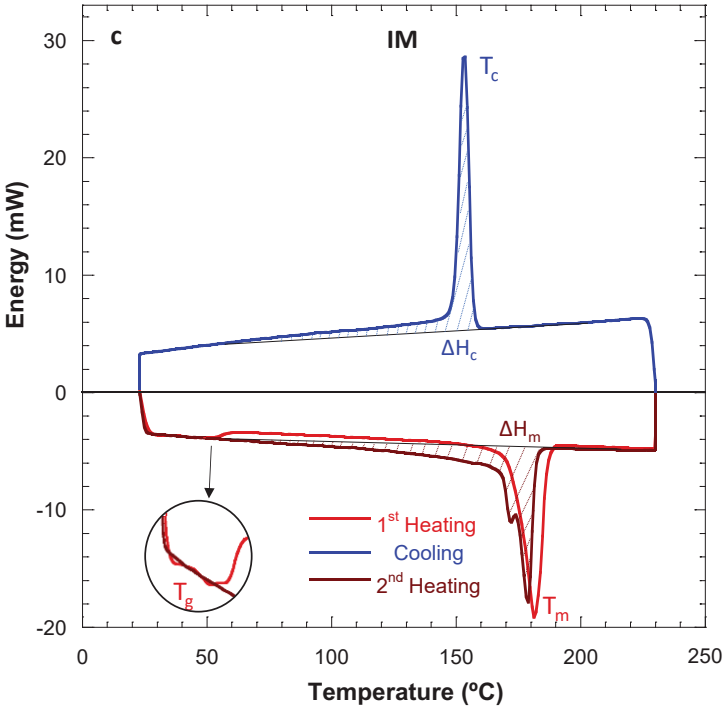
c
IM
T_c
ΔH_c
ΔH_m
T_g
T_m
1st Heating
Cooling
2nd Heating
Energy (mW)
Temperature (ºC)
30
20
10
0
-10
-20
0
50
100
150
200
250

Table 5-4. Thermal properties obtained from DSC tests in SLS PA-12 specimens with different orientations and IM PA-12 samples.

	T_g(°C)	T_c(°C)	T_m(°C)	X_c (%)	X_m (%)
				34.4	31.1
SLS 0° orientation	55.4	137.7	183.1	**Average**	
				32.8 ± 2.3	
				34.7	30.7
SLS 90° orientation	54.6	140.2	184.0	**Average**	
				32.7 ± 2.8	
				37.1	36.8
IM	50.6	151.3	180.7	**Average**	
				37 ± 0.2	

The thermal properties of *SLS* PA-12 at 0° and 90° orientations are almost identical, indicating that specimens at both orientations must have cooled at similar rates to give such consistent levels of crystallinity and temperatures. However, some differences were observed when comparing with *IM* PA-12. Specifically, *IM* specimens showed lower T_g, T_m and crystalline degrees, χ_c and χ_m, but higher T_c than *SLS* specimens. Once again, these differences are to do with the thermal history during the manufacturing process [165].

Dynamic Mechanical Analysis (*DMA*) gave information about the loss modulus, the storage modulus and the loss factor (*tanδ*). *Figure 5-5* shows the evolution of these parameters from -110 °C to 170 °C for *SLS* PA-12 at 0° orientation in *Figure 5-5.a*, for *SLS* PA-12 at 90° orientation in *Figure 5-5.b* and for *IM* PA-12 in *Figure 5-5.c*. The storage modulus plot gives a full picture of the load-bearing characteristics of the material as a function of changes in temperatures, while *tanδ* curves identify the regions where relatively large changes in properties occur over relatively narrow bands of temperatures and, consequently, related with material transition stages. Two obvious transitions at the ranges between 50 °C and 60 °C and between -60 °C and -70 °C are found independently of the processing technique in *Figure 5-5*. They are defined as the α and β relaxations, respectively.

As known, the α-relaxation corresponds to the glass transition temperature, T_g, and displays the peak of greatest magnitude. The α-relaxation results from the rupture of hydrogen bonds between polymeric chains, which gives rise to the motion of long-chain segments in the amorphous region [165], [166]. On

the other hand, the β-relaxation reflects the mobility of local hydrogen-bonded amide groups in the amorphous region and its appearance indicates that the material has good low temperature flexibility and cold endurance [165], [167]. *Table 5-5* collects the glass transition temperature and the β-transition

Figure 5-5. Thermal scans obtained from DMA tests containing the Storage Modulus, the Loss Modulus and the tanS from -110 °C to 170 °C for: (a) SLS PA-12 at 0° orientation (b) SLS PA-12 at 90° orientation and (c) IM PA-12.

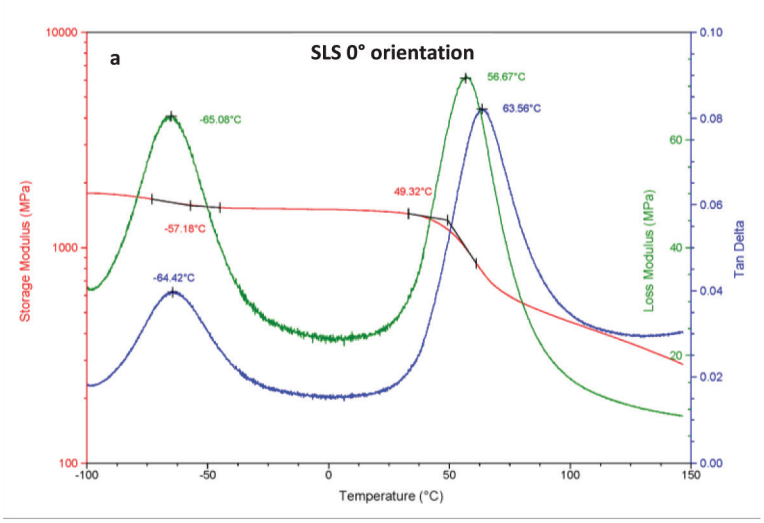

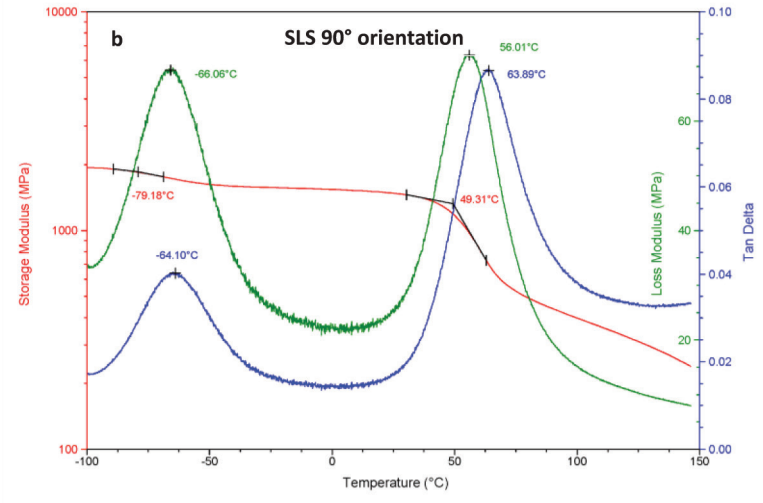

Figure 5-5. Thermal scans obtained from DMA tests containing the Storage Modulus, the Loss Modulus and the tanS from -110 °C to 170 °C for: (a) SLS PA-12 at 0° orientation (b) SLS PA-12 at 90° orientation and (c) IM PA-12. (Continued)

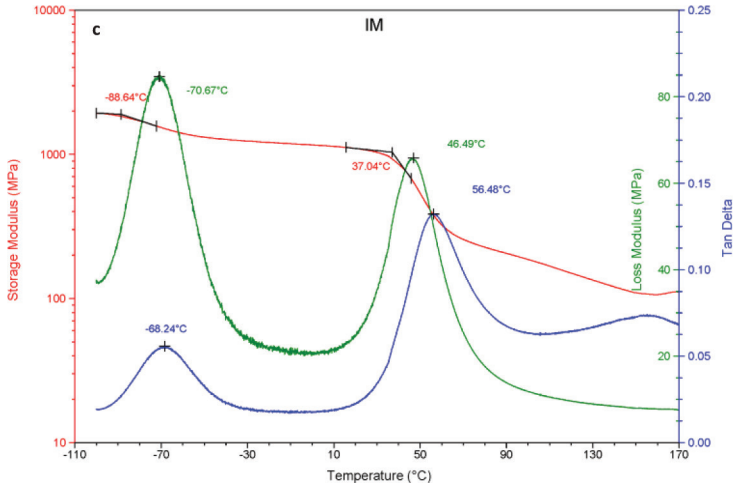

Table 5-5. Transition temperatures, T_α and T_β and storage modulus at room temperature obtained from DMA tests for IM PA-12 and for SLS PA-12 at 0° and 90° orientations.

	T_α (°C)	T_β (°C)	Storage modulus at 23°C (MPa)
SLS 0° orientation	63.6	-64.4	1472
SLS 90° orientation	63.9	-64.1	1488
IM	56.5	-68.2	1084

temperature determined from the peaks of the *tan δ* curves. Firstly, these transitions are similar for both orientations in *SLS* specimens, confirming the no dependency with the manufacturing orientation. Nevertheless, both the glass transition temperature and the β-transition temperature in *IM* specimens shift to lower temperatures. This also occurred in *DSC* measurements *(Table 5-4)*. The reason might be the faster crystallisation in the *IM* process, causing an amorphous phase with more irregularly arranged molecular chain and better mobility, thus implying lower values of T_α and T_β [168].

Table 5-5 also shows the storage modulus at room temperature. As in other properties, there is no influence of the orientation on the storage modulus in *SLS* PA-12, but the value of the *IM* PA-12 specimens was almost 40% lower than the values of the *SLS* PA-12 samples. It is well settled that the Young's

Figure 5-6. Characteristic engineering stress-strain curves at -50 °C, 23 °C and 50 °C obtained from tensile tests in SLS PA-12 at 0° orientation.

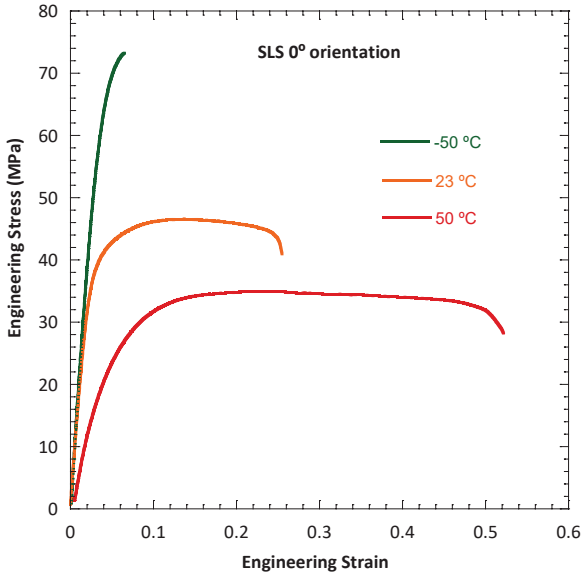

Figure 5-7. Characteristic engineering stress-strain curves at -50 °C, 23 °C and 50 °C obtained from tensile tests in SLS PA-12 at 90° orientation.

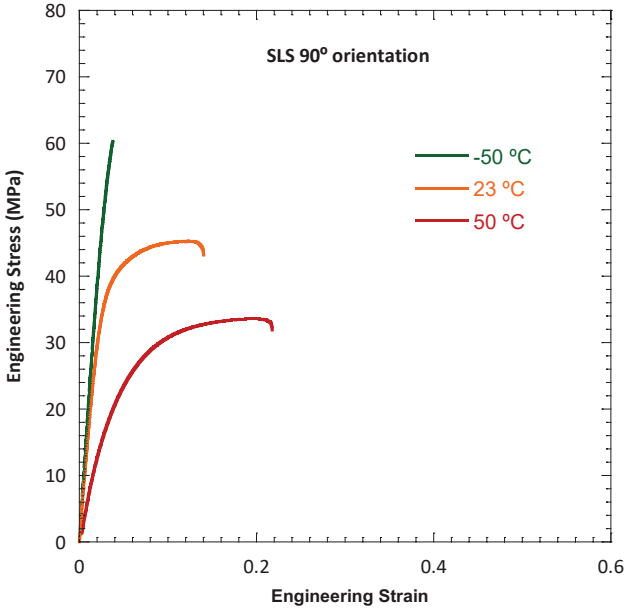

moduli increase with the crystallinity degree [169], but the opposed behaviour observed in this case may be due to the presence of a no negligible skin layer of amorphous material together with a much smaller spherulitic structure.

5.5 Mechanical properties

Figure 5-6 and *Figure 5-7* show characteristic engineering stress-strain curves of *SLS PA-12* at 0° and 90° orientations, respectively, obtained from tensile tests at -50 °C, 23 °C and 50 °C. As expected, the mechanical response is strongly influenced by the temperature. At -50 °C, above T_β, *SLS* at 0° and 90° orientation presented semi-brittle behaviour due to the activation of mobility of side groups of the chain. For temperatures above T_g, that is, at 23 °C and 50 °C, the material displayed a ductile behaviour. As usually, the ductility decreased but the stiffness and the strength increased as the temperature reduced.

Figure 5-8 analyses the effect of orientation and manufacturing process on the tensile behaviour, showing clear differences. Firstly, *SLS* PA-12 presented

Figure 5-8. Characteristic engineering stress-strain curves at 23 °C obtained from tensile tests of IM PA- 12 and of SLS PA-12 at 0° and 90° orientations.

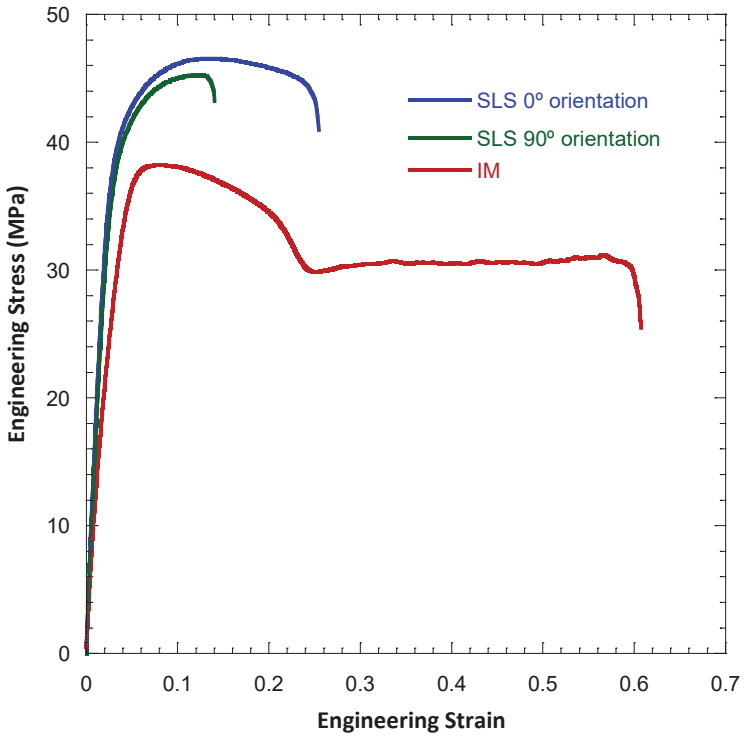

Figure 5-9. Evolution of the Young's modulus with temperature in SLS PA-12 at 0° and 90° orientations and with the manufacturing process at 23 °C.

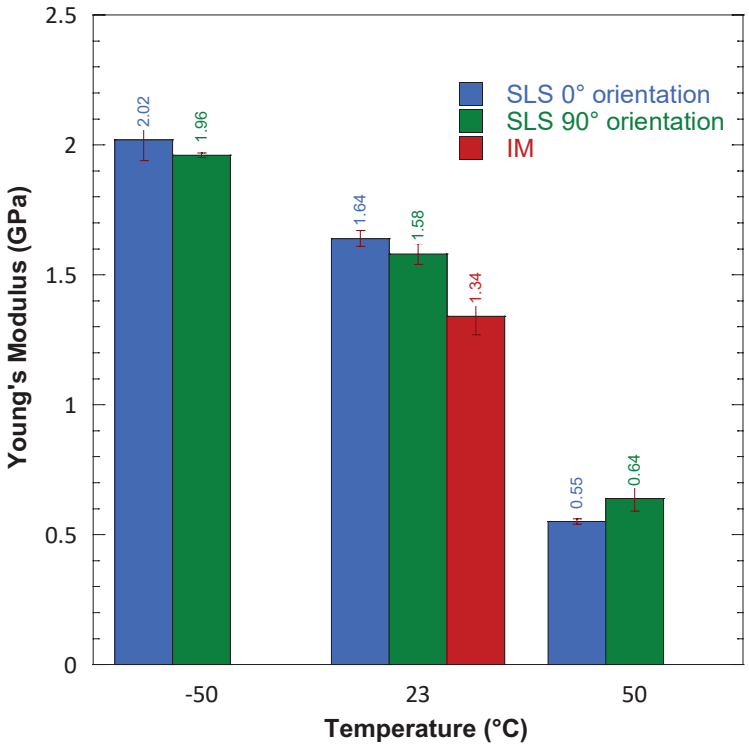

higher strength and stiffness but lower ductility than *IM* PA-12. In addition, it is easily observed that in *SLS* material, the mechanical response at both orientations is similar except for the ductility.

Figure 5-9, Figure 5-10, Figure 5-11 and *Figure* 5-12 show the evolution of Young's modulus, tensile strength, elongation at break and Poisson's ratio with temperature, orientation and manufacturing process, respectively. Regarding Young's modulus *(Figure 5-9),* the values decrease with the temperature increase, being this reduction more accentuated at 50 °C, due to the nearness to T_g (*Table 5-4*).

For *SLS* PA-12, there were hardly differences in the Young's modulus with the orientation for the same temperature. On the other hand, *IM* PA-12 exhibited the lowest Young's modulus at room temperature, being 20% lower than the larger one corresponding with *SLS* PA-12 at 0° orientation.

Figure 5-10. Evolution of the tensile strength with temperature in SLS PA-12 at 0° and 90° orientations and with the manufacturing process at 23 °C.

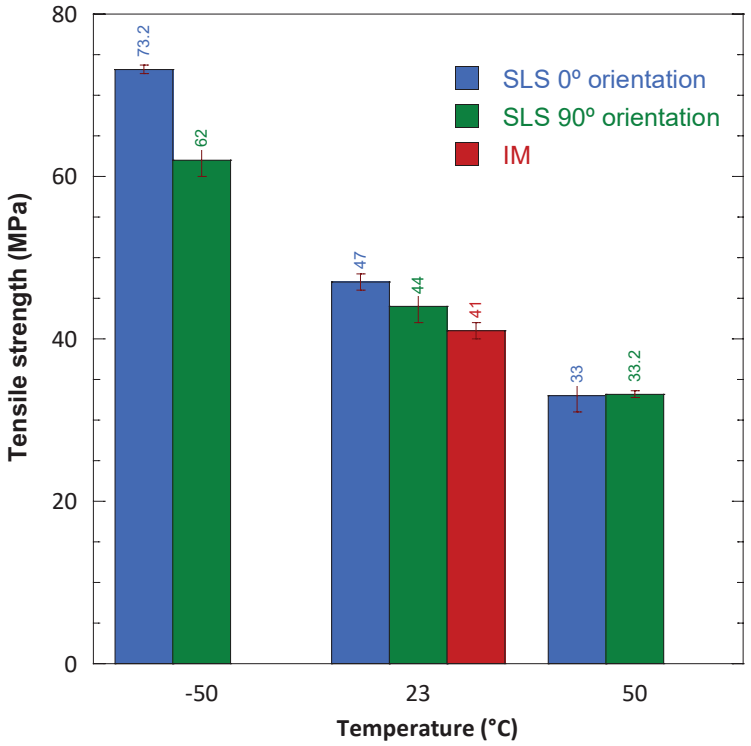

The tensile strength followed the same trend as the Young's modulus *(Figure* 5-10): the higher the temperature, the lower the tensile strength at both orientations in *SLS* PA-12, and the lowest value at room temperature was obtained for *IM* PA-12. Concerning the orientation, *SLS* PA-12 at 0° orientation showed higher values than at 90° orientation, but the differences reduced as the temperature rose till reaching similar values at 50 °C.

When analysing the influence of the temperature on the elongation at break (*Figure 5-11*) in *SLS* PA-12, the values of this parameter increases with temperature rising independently of the orientation. Nevertheless, the elongation at break at 0° orientation was more elevated than at 90° orientation at any temperature, registering the higher difference at 50 °C, with values at 0° orientation 3 times larger than those at 90° orientation. The proximity of 50 °C to the T_g of the material was the reason of this significant increase because the mobility of large scale coordinated motions of the polymer chains occurs, resulting in a massive relaxation of the material. At room temperature, the

Figure 5-11. Evolution cf the elongation at break with temperature in SLS PA-12 at 0° and 90° orientations and with the manufacturing process at 23°C.

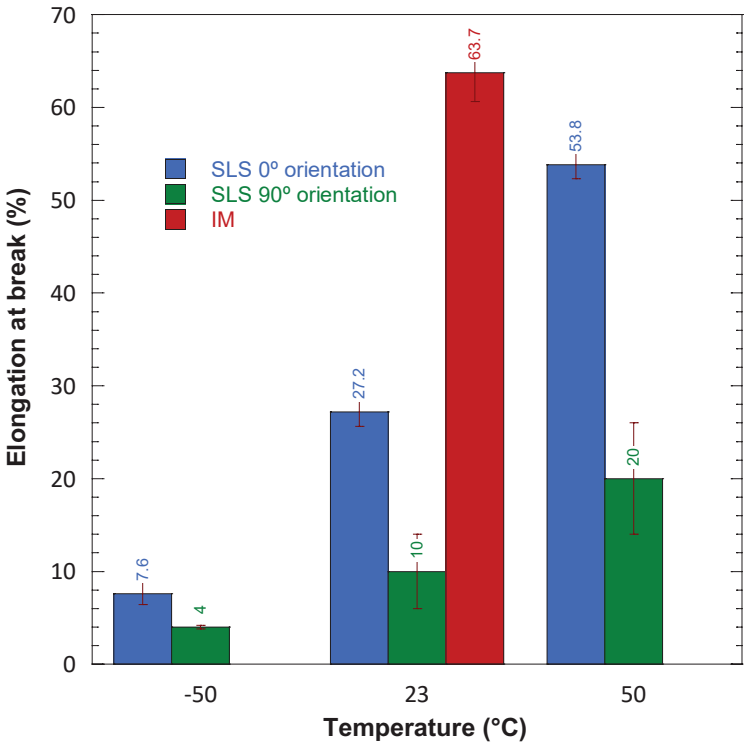

elongation at break of *IM* PA-12 is more than twice the value measured in *SLS* PA-12 at 0° orientation.

Regarding the Poisson's ratio, *Figure* 5-12 shows increments with temperature, having the 0° orientation the largest value for *SLS* PA-12 at the three tested temperatures but being overtaken by the value of *IM* PA-12 at room temperature.

These results match with the existing bibliography (*section 2.2.1, Table 2-1)*. Firstly, the Young's modulus and the tensile strength of *IM* PA-12 were smaller than those of *SLS* PA-12 despite the higher crystallinity degree of the former (Table 5-4). *Crist et al.* [141], [169] stated the opposite trend, the higher the crystallinity degree the higher the elastic modulus and the tensile strength. Nevertheless, the presence of an amorphous skin layer with significant dimensions in the *IM* PA-12 is an important factor to have in mind. Also, a different spherulite size between *SLS* PA-12 and *IM* PA-12 seems to affect the elongation at break [170]. Results obtained in *SLS* specimens at 23°C are

Figure 5-12. Evolution of the Poisson's ratio with temperature in SLS PA-12 at 0° and 90° orientations and with the manufacturing process at 23 °C.

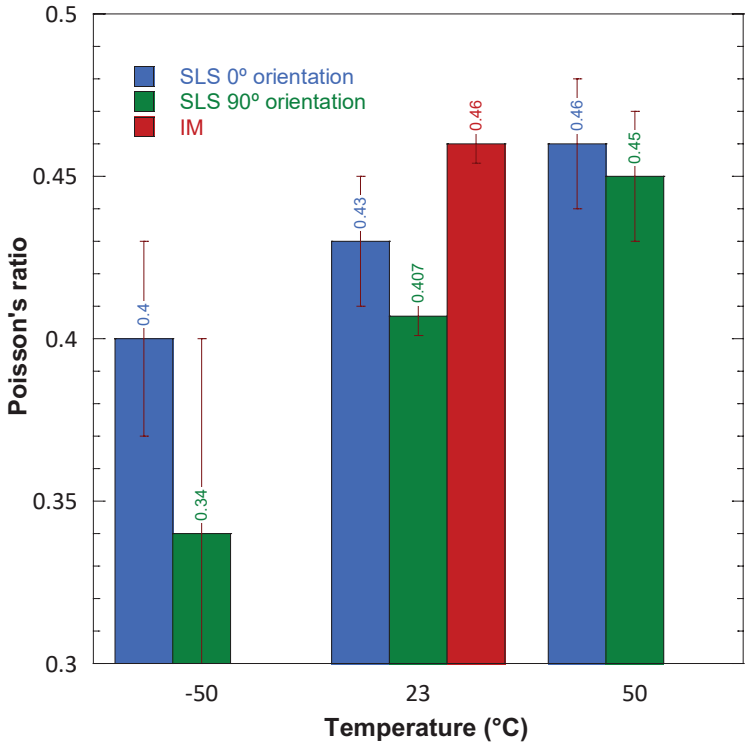

analogous to those of Seltzer et al. [31], Caulfied et al. [33], Stichel et al. [34], Munguia et al. [118], [119], Xu et al.[161], Mousa [171] and Hao et al. [172]. Finally, the results obtained in *IM* PA-12 are comparable to those reported by Hooreweder et al. [30].

5.5.1 Tensile tests fractographies

SEM fractographies were taken from the fracture surfaces of the tensile test specimens to study the effect of temperature, orientations and manufacturing processes, identifying the micromechanisms of deformation and fracture.

Figure 5-13 and *Figure 5-14* show the fracture surfaces at -50 °C, 23 °C and 50 °C of *SLS* PA-12 at 0° and 90° orientations, respectively. The common trend observed in both orientations was an increment in the surface smoothness with lower temperatures. However, there are several differences between the *SLS* orientations.

Figure 5-13. Fracture surfaces from tensile tests of SLS PA-12 at 0° orientation at different temperatures: (a) -50°C, (b) 23°C and (c) 50°C.

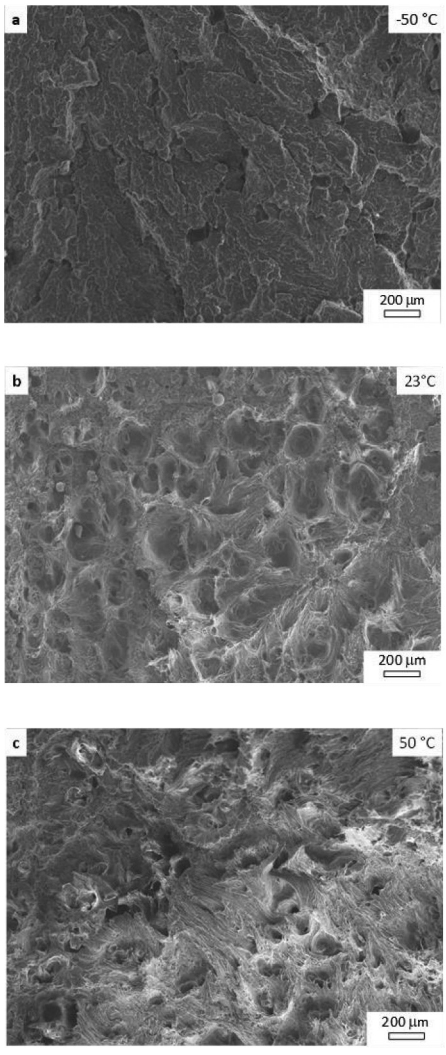

Figure 5-14. Fracture surfaces from tensile tests of SLS PA-12 at 90° orientation at different temperatures: (a) -50°C, (b) 23°C and (c) 50°C.

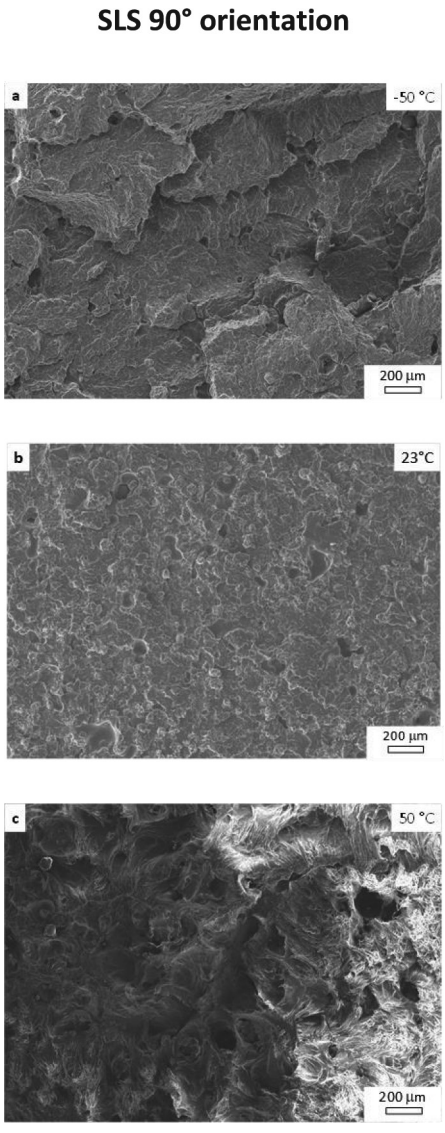

There is no influence of the orientation on the morphology of the fracture surfaces at -50 °C *(Figure 5-13.a* and *Figure 5-14.a*). The morphology was irregular, identical to those observed by other authors [173]. The similarity of

the fracture morphology is consistent with the values of the tensile parameters, specially the elongation at break (*Figure* 5-11), which were identical at this low temperature for both orientations.

At 23 °C *(Figure 5-13.b* and *Figure 5-14.b*), the fracture surface at 0° orientation is much rougher than those resulting from tests at -50 °C, being characterized by the presence of voids surrounded by amorphous filaments of PA-12, which had been stretched and finally broken along the crack growth direction. These features are associated with the nucleation, growth and coalescence of crazes, which is a phenomenon commonly observed in thermoplastic polymer fractures [174].

The nucleation site could be at defects as pores or interspherulitic areas. The stretched filaments surrounding voids are displayed in *Figure 5-15*. On the other hand, the 90° orientation exhibits a plain surface with no evidence of plastic deformation of filaments but where pores and unmolten particles are discernible. This distinct morphologies at different loading directions are in accordance with the elongation at break values (*Figure* 5-11*)*, specifically the increase in surface roughness goes hand in hand with the increase in the elongation at break.

Finally, the fractographies of specimens tested at 50 °C (*Figure 5-13*.c and *Figure 5-14.c*) show a much higher ductile deformation of the amorphous filaments than at 23 °C, and when comparing the orientations, the specimens tested at 0° orientation presented more tearing than at 90° orientation. In this case, the ductile behaviour is enhanced with the closeness to the material T_g (*Table 5-4*). The high mobility of the molecular boosts the ductile tearing along the load direction at both orientations. Once again, this fractographic morphologies agree with the elongation at break results (*Figure* 5-11), which are the highest of all the tested temperatures and with values at 0° orientation more than twice those measured at 90° orientation.

To determine the effect of the processing technique, *Figure 5-16* shows the fracture surface of *IM* PA-12. The panoramic view *(Figure 5-16.a)* evidences that the failure starts at a surface defect (outlined in black dashed line) followed by macroscopic plastic deformation of the gage length with the formation of a necking zone which propagates along the specimen. The high level of plastic deformation undergone by the amorphous filaments is in agreement with the high values of elongation at break (*Figure 5-11)*. The detailed view *(Figure 5-16.b*) clearly denotes the stretched gage length broken after ductile tearing.

Moreover, there is complete lack of defects in form of pores or unmolten particles. Therefore, the crazing mechanism together with the presence of internal defects may be the reason why the ductility at failure of the *SLS* PA-12 is much lower than that of *IM* PA-12 [168].

Figure 5-15. Detail of crazing mechanism: voids surrounded by amorphous stretched and broken PA-12 filaments.

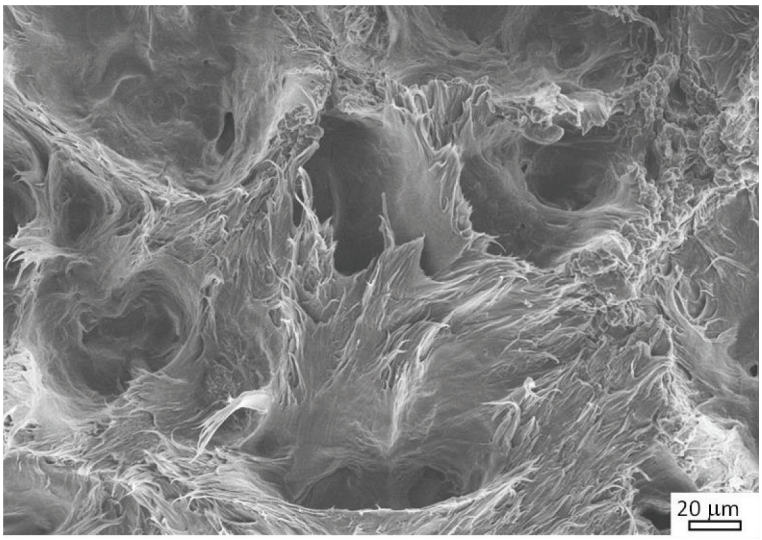

Figure 5-16. Fracture surfaces from tensile tests of IM PA-12 at 23°C: (a) panoramic view with the surface defect starter cf failure delimited with a dotted line, (b) detail cf ductile tearing.

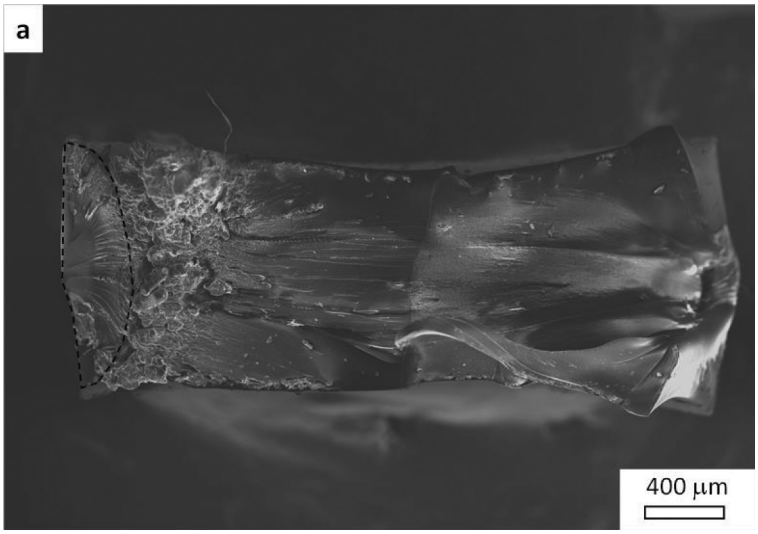

5.6 Fracture behaviour

For the determination of the fracture parameters, different approaches were applied depending on the mechanical response of the material at each experimental condition as described in the *section 4.6.2*.

Figure 5-17 shows the representative load-displacement records obtained from fracture tests at -50 °C of *SLS* PA-12 at 0° and 90° orientations. Despite the semi-brittle behaviour, all the requirements of the *LEFM* approach were fulfilled, so the recommendations of ISO 13856 standard [149] were followed to determine the critical stress intensity factor, K_{IC}, and the critical energy release rate, G_{IC}.

Figure 5-18 displays the representative load-displacement records obtained from fracture tests at 23 °C of *IM* PA-12 and of *SLS* PA-12 at 0° and 90° orientations.

Figure 5-17. Representative load-displacement curves obtained from fracture tests at -50 °C of SLS PA- 12 at 0° and 90° orientations.

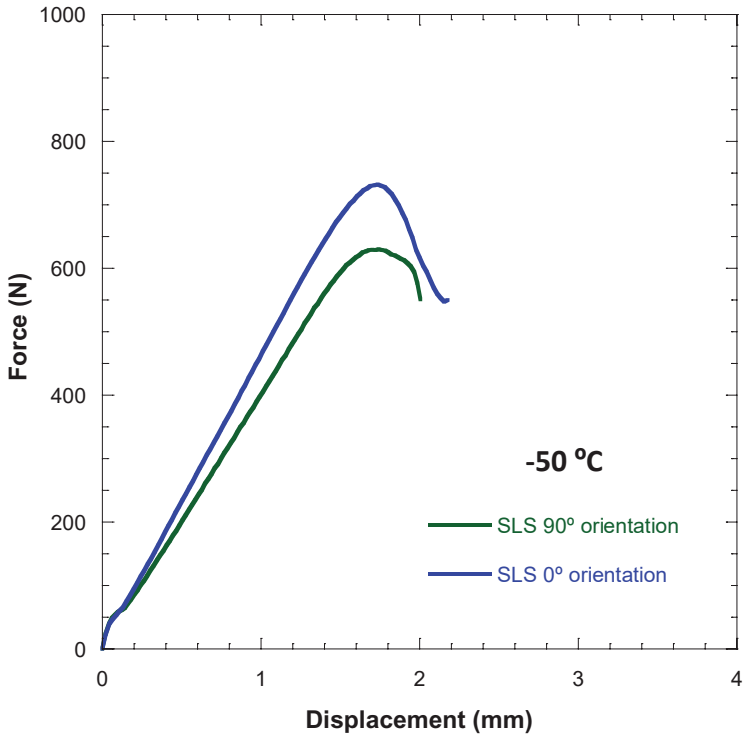

Figure 5-18. Representative load-displacement curves at 23 °C obtained from fracture tests of IM PA-12 and of SLS PA-12 at 0° and 90° orientations.

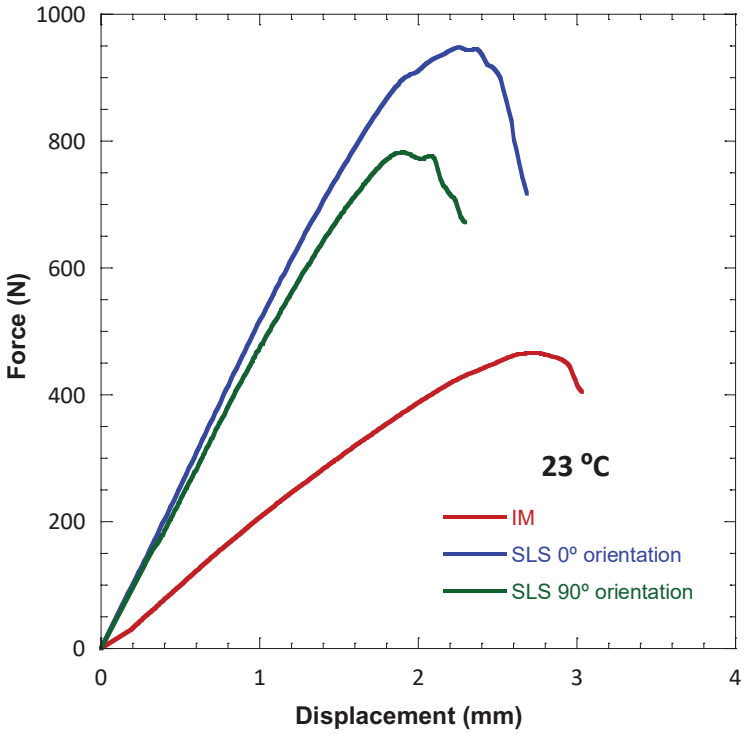

The difference in stiffness is mainly due to the different initial crack lengths. The behaviour of *IM* PA-12 specimens and both orientations of *SLS* PA-12 samples was also semi-brittle but, at this temperature, not all the tests verified the linearity criterion, because there were some tests which deviated from the linearity, as the $\frac{P_{max}}{P_Q}$ ratio exceeded narrowly 10%. Therefore, the two approaches, *LEFM* and *NLFM*, were applied at 23 °C despite most of the tests complied with the *LEFM* requirements. The normalization method described in ASTM E1820 standard [150] was followed to determine the J-R curve and the energy at crack growth initiation, J_{IC}, and the G_{IC} values provided by *LEFM* were also calculated.

Finally, *Figure 5-19* includes the representative load-displacement records of the fracture test at 50 °C of *SLS* PA-12 at 0° and 90° orientations. The nonlin-

Figure 5-19. Representative load-displacement curves at 50 °C obtained from fracture tests cf SLS PA-12 at 0° and 90° orientations.

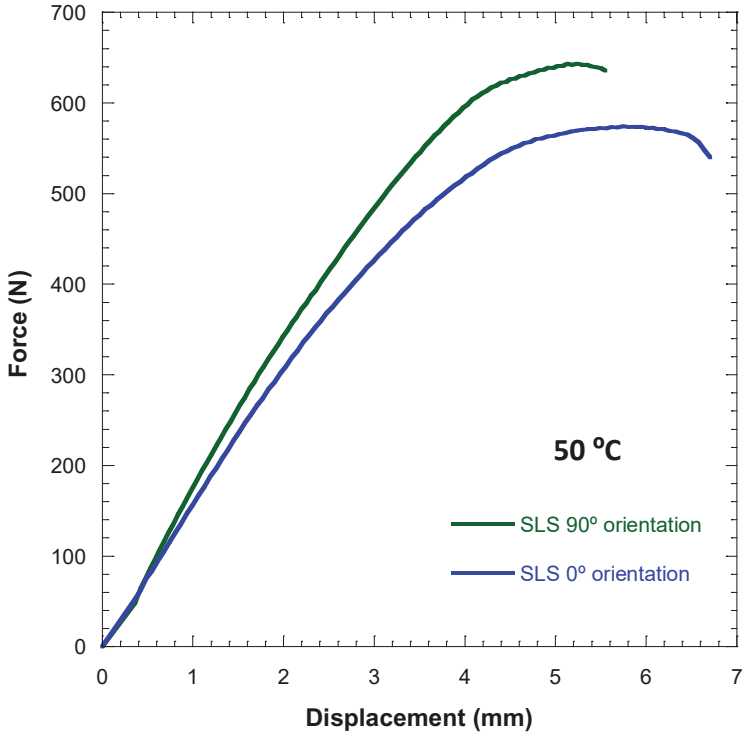

earity was so high that the application of *NLFM* approach was undoubtful and the normalization method was used to determine the J-R curve and J_{IC} values.

Figure 5-20 shows the evolution of the fracture toughness in terms of the stress intensity factor, K_{IC}, when computable, with the temperature, the load orientation for *SLS* PA-12 and the manufacturing technique. Firstly, all the values were in plane strain conditions. As expected, K_{IC} values decrease as the temperature increases in *SLS* PA-12. Regarding the effect of the orientation, the values of K_{IC} obtained at 90° orientation were lower than at 0° orientation. The values of K_{IC} at 23 °C computed in this investigation were comparable to those obtained by Seltzer et al. [31] and by Salazar et al. [39], but higher than those obtained by Linul et al. [46]. The discrepancy in this case has to do with the low density of the parts measured by the latter, correlated with the values of the manufacturing parameters employed.

Attending to the effect of the manufacturing technique at 23 °C, no differences between *IM* PA-12 and *SLS* PA-12 results were found.

Figure 5-20. Fracture toughness cf SLS PA-12 at 0° and 90° orientations determined at -50 C and at 23°C and of IM PA-12 at 23°C.

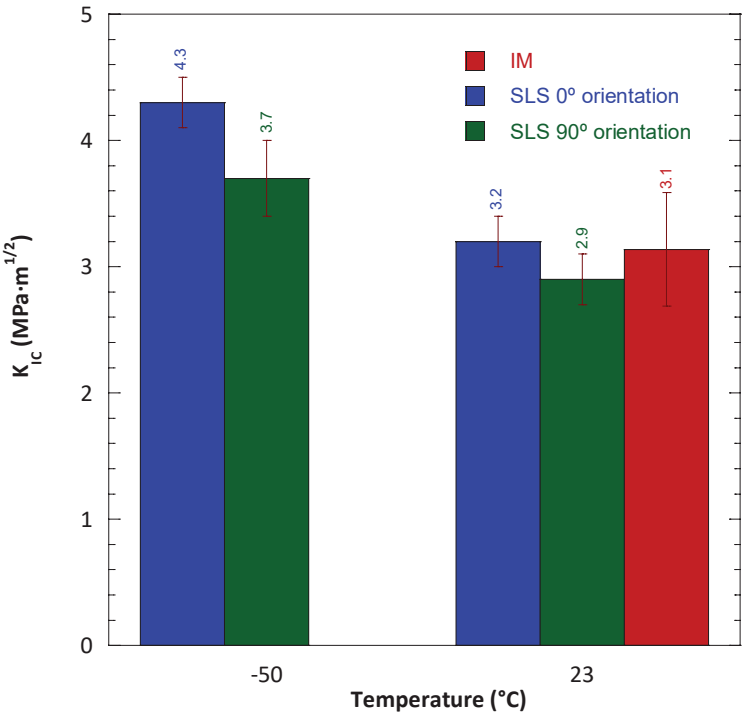

Within the computation of the fracture parameters under the *NLFM* approach, *Figure 5-21* and *Figure 5-22* show the J-R curves at 23 °C and 50 °C of SLS PA- 12 at 0° and 90° orientations, respectively. Firstly, the J-R curves at 50 °C were all above those at 23 °C independently of the load direction with respect to the layered structure. Secondly, for the very same temperature, the J-R curves of *SLS* PA-12 at 0° orientation were above and steeper than those of *SLS* PA-12 at 90° orientation.

To investigate the effect of the manufacturing process, *Figure 5-23* compares the J-R curves at 23 °C of *SLS* PA-12 at 0° and 90° orientations with those obtained from *IM* PA-12. Firstly, regarding *SLS* materials, the energy needed to produce the stable crack growth at 0° orientation is higher than that at 90° orientation, being the latter less resistant against crack growth. Secondly, the J-R curves of *IM* PA-12 presented a high dispersion but in average the behaviour was in between that of *SLS PA-12* at 0° orientation and that of *SLS PA-12* at 90° orientation.

Figure 5-21. Influence cf the temperature in SLS PA-12: J-R curves at 23 °C and 50 °C cf SLS PA-12 at 0° orientation.

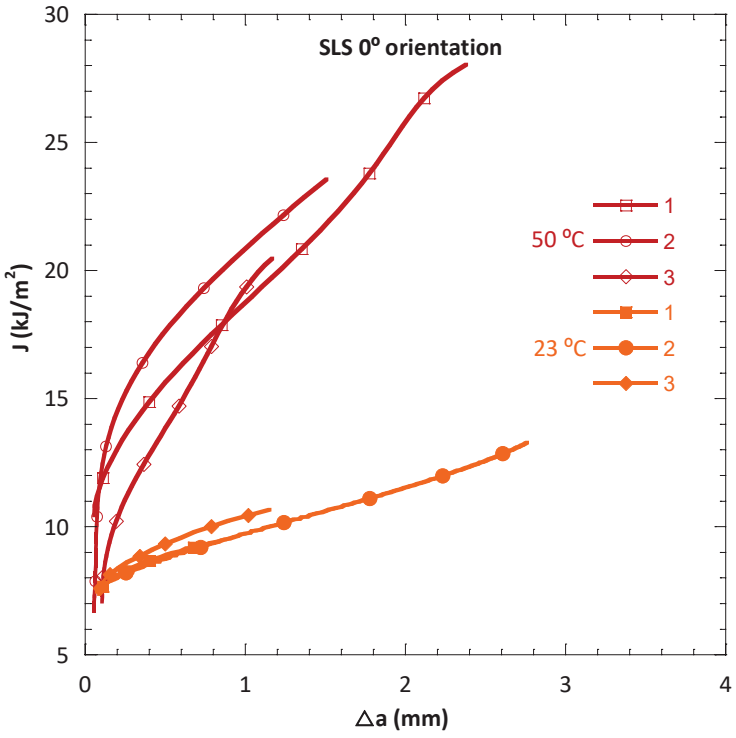

Table 5-6 collects the quantification of all these differences, more specifically, the values of the exponent N_J and of the parameter C_J of the potential law with the form $J = C_J \Delta a^{N_J}$ which has been used to fit the experimental values. Firstly, the exponent N_J and the parameter C_J increased when the temperature increased at both orientations of *SLS* PA-12. Secondly, at the same temperature, the higher values of the exponent N_J of *SLS* PA-12 at 0° orientation in comparison with those of *SLS* PA-12 at 90° orientation confirm the trend observed graphically.

Finally, although *IM* PA-12 exhibits an average behaviour between that of *SLS* PA-12 at 0° orientation and that of *SLS* PA-12 at 90° orientation, the curves were more like those of *SLS* PA-12 at 90° orientation, implying similar N_J coefficients.

Figure 5-24 shows the energy at crack growth initiation, J_{IC} and G_{IC}, as a function of temperature, orientation for *SLS* PA-12 and processing technique

Figure 5-22. Influence cf the temperature in SLS PA-12: J-R curves at 23 °C and 50 °C cf SLS PA-12 tested at 90° orientation.

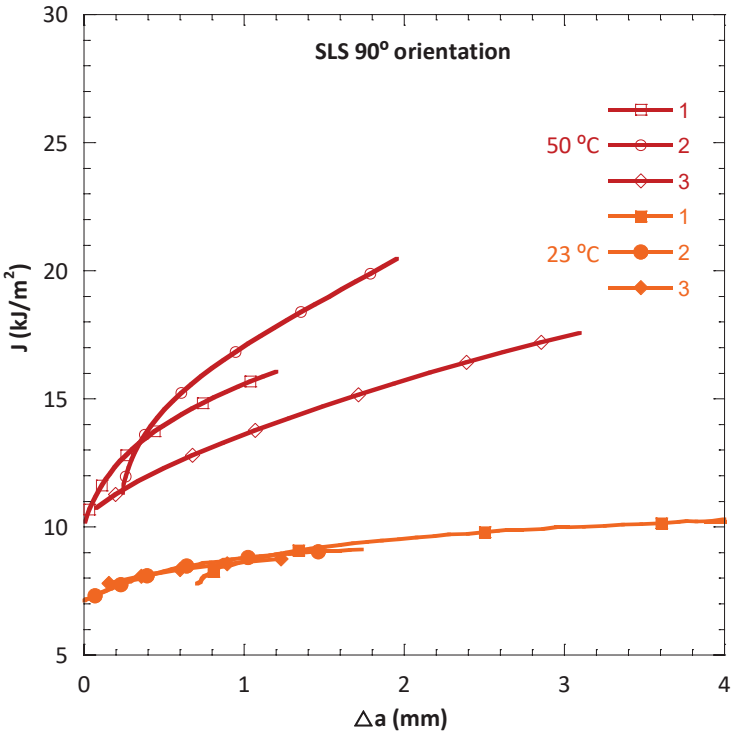

at 23 °C. Regarding the effect of the temperature in *SLS* PA-12, there is an important increment in the J_{IC} values obtained at 50 °C, which nearly doubled those at 23 °C.

This behaviour can be explained considering that 50 °C is close to the T_g of the material (*Table 5-4*), so the viscous state plays a notable role in the fracture behaviour, requiring more energy for crack growth initiation.

It can be remarkable the similarity of G_{IC} and J_{IC} obtained at 23 °C for *SLS* PA-12 at 0° and 90° orientations, without statistical differences between them. Meanwhile at -50 °C and at 50 °C, the fracture energy of *SLS* PA-12 at 0° orientation is higher than that of *SLS* PA-12 at 90° orientation.

Finally, the values of G_{IC} and J_{IC} of *IM* PA-12 were higher than those of *SLS* PA- 12, showing the best crack growth initiation resistance.

Table 5-6. Fitting values of the experimental J-R curves to the power law equation $J = C_J \Delta a^{NJ}$ at 23 °C and 50 °C of SLS PA-12 tested at 0° and 90°orientations and of IM PA-12 tested at 23 °C.

	***SLS* 0° orientation**			***SLS* 90° orientation**			***IM***		
	Specimen ID	C_J	N_I	**Specimen ID**	C_J	N_J	**Specimen ID**	CJ	NJ
23 °C	**1**	9.53	0.01	***1***	8.56	0.14	***1***	9.70	0.07
							2	9.74	0.08
	2	10.3	10.3	***2***	8.61	0.06	***3***	11.22	0.09
							4	10.25	0.05
							5	7.52	0.17
	3	10.2	0.18	***3***	8.66	0.06	***6***	10.84	0.15
							7	8.32	0.12
	Average	10.0 ± 0.4	0.14 ± 0.04	***Average***	8.61 ± 0.05	0.08 ± 0.05	***Average***	9.6 ± 1.3	0.10± 0.04
50 °C	**1**	20.1	0.26	***1***	15	0.1			
	2	21.7	0.31	***2***	14	0.14			
	3	18.8	0.40	***3***	17	0,25			
	Average	20.2 ± 1.5	0.32 ± 0.07	***Average***	15.3 ± 1.5	0.13 ± 0.09			

Figure 5-23. Influence of the manufacturing process at 23 °C: J-R curves of SLS PA-12 at 0° and 90° orientations and of IM PA-12.

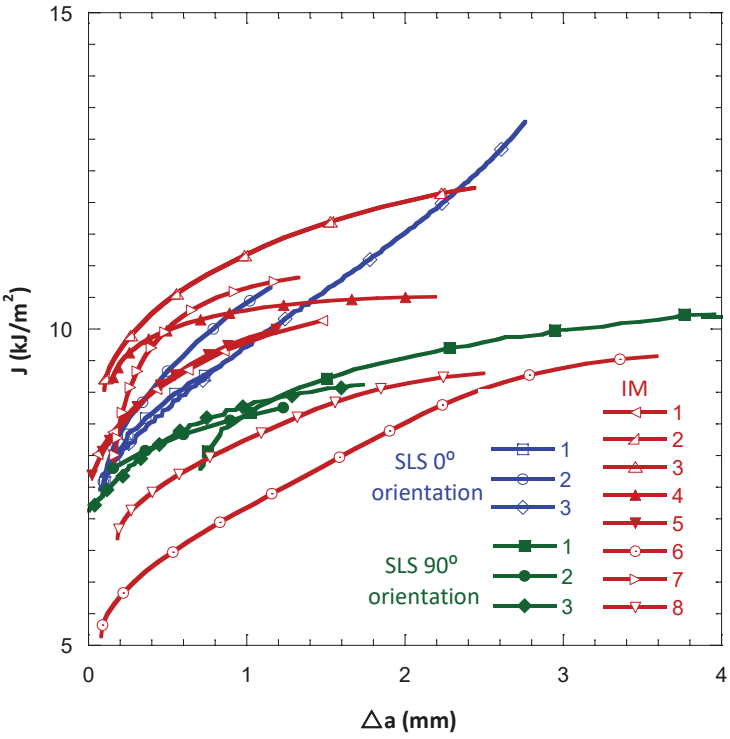

5.6.1 Fractographic analysis of fracture tests

Figure 5-25 and Figure 5-26 display the fracture surfaces obtained from fracture tests carried out at -50 °C, 23 °C and 50 °C of *SLS* PA-12 at 0° and 90° orientations, respectively. It is important to mention that all *SLS* PA-12 fracture surfaces presented defects in form of pores or unmolten powder particles.

Independently of the orientation, the morphology of the fracture surfaces at -50 °C *(Figure 5-25.a* and *Figure 5-26.a*) and at 23 °C *(Figure 5-25.b* and *Figure 5-26.b*) presented small differences. The characteristic feature is a patchwork pattern with more evident deformed borders at 23 °C. However, at 50 °C the degree of plastic deformation is more pronounced with presence of voids

However, at 50 °C the degree of plastic deformation is more pronounced with presence of voids through the ductile tearing of the amorphous filaments along the crack propagation direction *(Figure 5-25.c* and *Figure 5-26.c*). This

Figure 5-24. Energy at crack growth initiation as a function of the testing temperature and the orientation in SLS PA-12. The influence of the manufacturing technique at 23°C is also displayed including the values obtained from IM PA-12 fracture specimens.

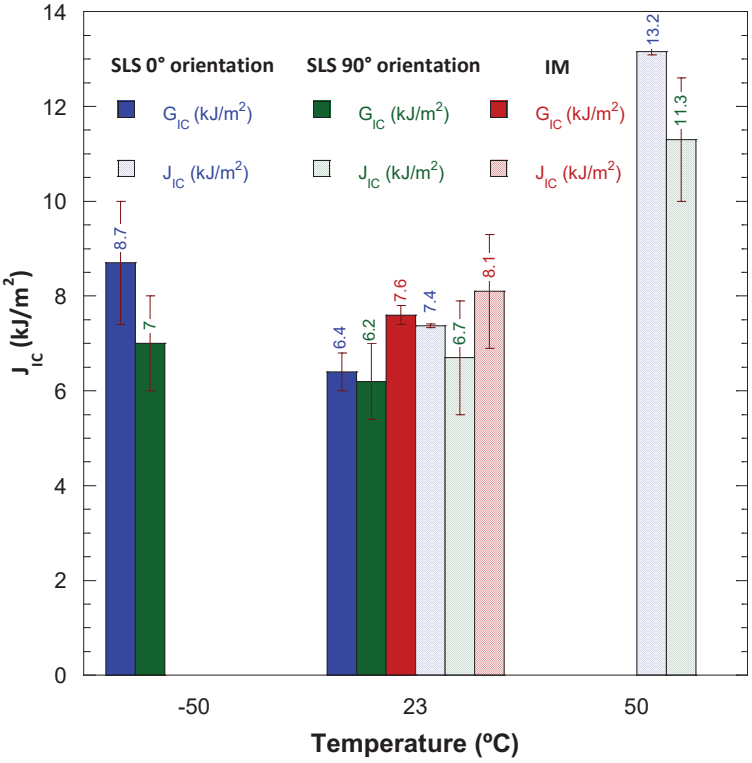

fractographic analysis agrees with the fracture toughness values collected in *Figure 5-24*.

No differences could be detected between the fracture surfaces of the *SLS* specimens tested at 0° and 90° orientations at all the testing temperatures. This fact matches with the indistinguishable values of the fracture energy at both orientations, except for those at 50 °C (*Figure 5-24*).

The dominant failure mechanism is crazing, characterized by the nucleation of microvoids followed by their growth (*Figure 5-27*) and final coalescence, leaving behind craters with more or less stretched amorphous filaments. The evolution of this damage mechanism during crack growth advancement leaves the patchwork pattern previously described. As the temperature rises, the dimples associated with crazing can be less visible due to the high elongation of surrounding filaments along the crack propagation direction.

Figure 5-25. Fracture surfaces of SLS PA-12 at 0° orientation tested at: (a) -50°C, (b) 23°C and (c) 50°C. The arrow shows the crack growth direction.

SLS 0° orientation

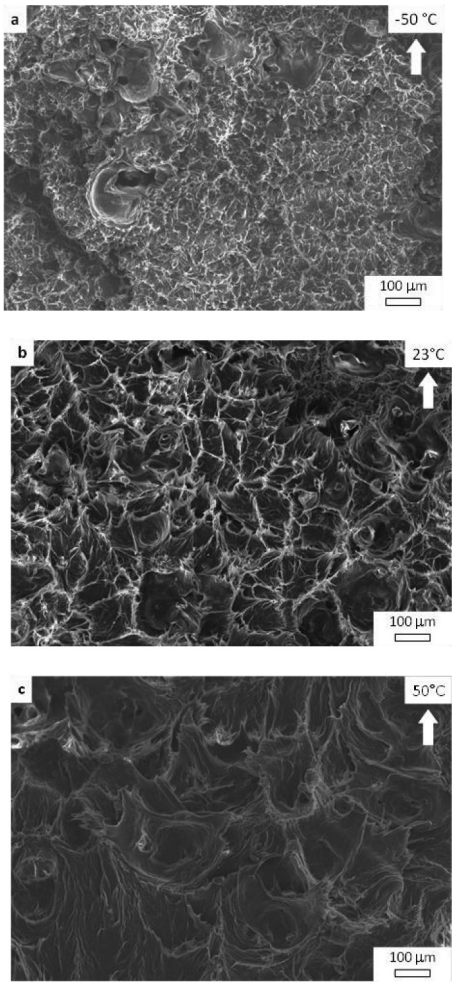

Figure 5-26. Fracture surfaces of SLS PA-12 at 90° orientation tested at: (a) -50°C, (b) 23°C and (c) 50°C. The arrow shows the crack growth direction.

SLS 90° orientation

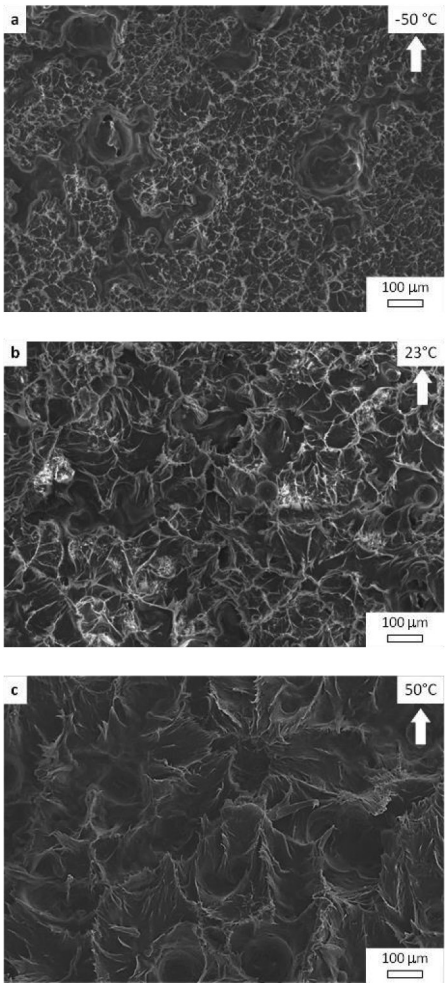

Comparing this fractographic morphology with the analysis carried out by Karger-Kocsis and Friedrich in injection molded polyamide 6.6 [80], the nucleation sites of the craze micromechanism could be related with defects as pores or unmolten particles as well as the crystalline structure.

Figure 5-27. Detail of "Crazes" observed at 23°C.

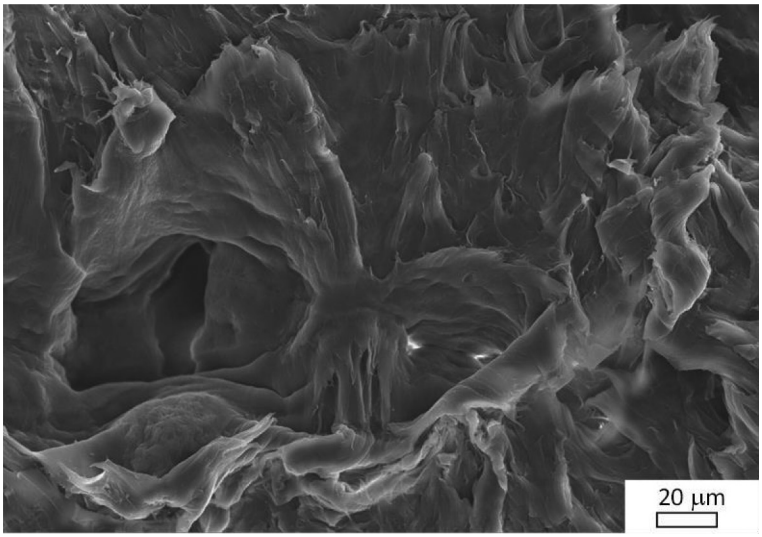

Figure 5-28. Fracture surface obtained from fracture tests cf IM PA-12 at 23°C.

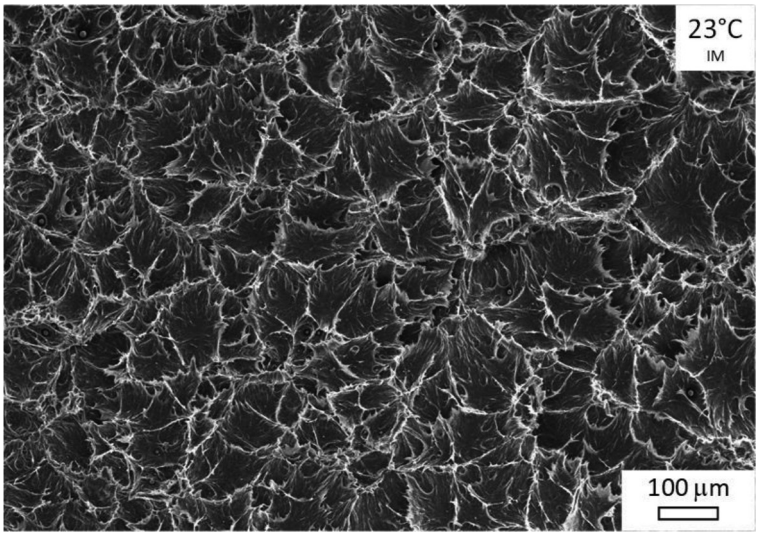

Figure 5-28 shows the fracture surface of *IM* PA-12. In this case, the patchwork pattern is much finer and more homogeneous than that observed in *SLS* PA-12 (*Figure 5-25* and *Figure 5-26*), and what is more, the fracture surfaces were free of unmolten particles or defects.

The finer size of the patch in the *IM* samples could be related to the small size of the crystalline structure (*Table 5-3*), together with the lack of processing defects, providing higher values of the fracture toughness (*Figure 5-24*). As stated by Salazar et al. [175], the decrease of the crystalline size favors the number and flexibility of the molecular chains in charge of holding together the lamellae bundles and consequently, improves the fracture energy. The reason is that the fracture toughness is governed, among other factors, by the energy required for the deformation and break of these tie molecules. Therefore, the higher the number of tie molecules, the higher the fracture energy.

5.7 Fatigue crack growth behaviour

Figure 5-29 shows the fatigue crack growth curves as a function of the control parameter $\Delta\sqrt{G}$ of *SLS* PA-12 at 0° orientation *(Figure 5-29.a)* and at 90° orientation *(Figure 5-29.b)*, and of *IM* PA-12 *(Figure 5-29.c)*. The log-log plots of $\frac{da}{dN}$ versus $\Delta\sqrt{G}$ graphs displayed in *Figure 5-29* only shows region II, a

Figure 5-29. Fatigue crack growth curves of PA-12 manufactured by SLS at (a) 0° orientation and (b) at 90°orientation and (c) by IM.

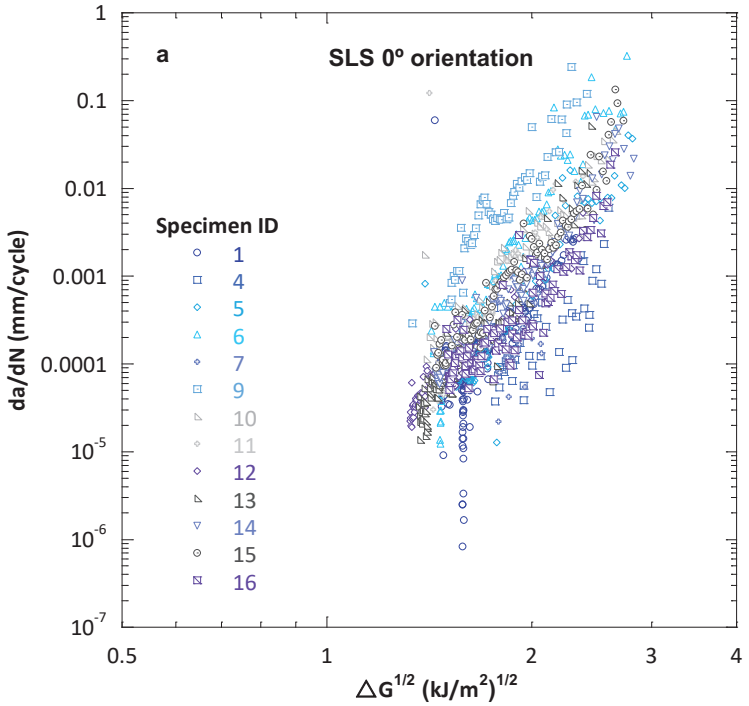

Figure 5-29. Fatigue crack growth curves of PA-12 manufactured by SLS at (a) 0° orientation and (b) at 90°orientation and (c) by IM. (Continued)

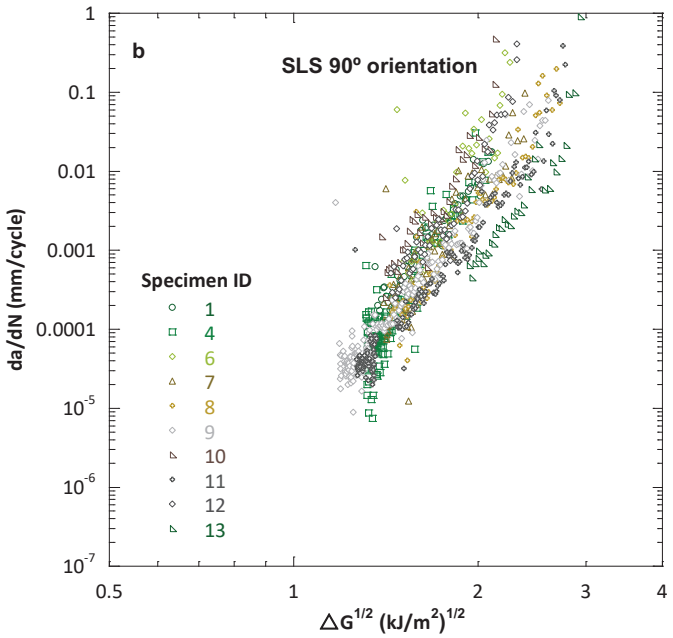

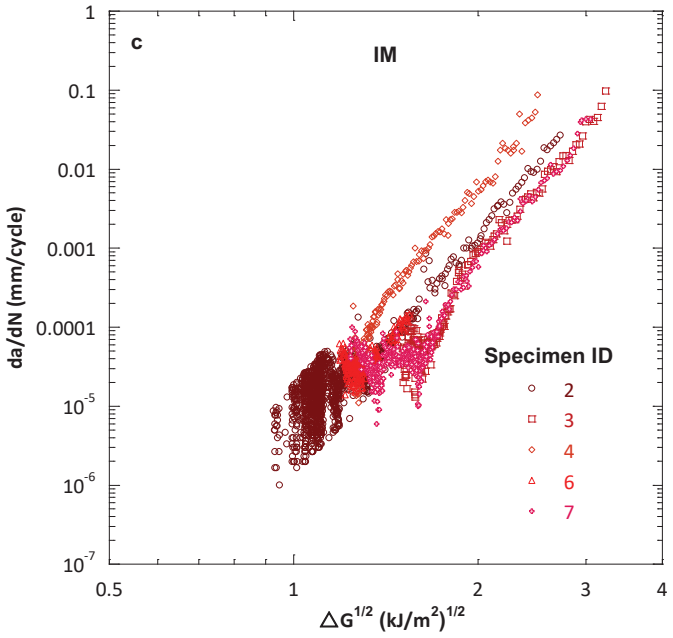

Table 5-7.Fatigue parameters of SLS PA-12 at 0° and 90° orientations and of IM PA-12. From $\Delta\sqrt{G}$ - decreasing tests, threshold values of the control parameter ($\Delta\sqrt{G}$)$_{th}$. From $\Delta\sqrt{G}$ -increasing tests average values of A and n parameters from Paris law (eq. (2-2)), maximum value of the crack driving force before break, ($\Delta\sqrt{G}$)$_{max,c}$, equivalent stress intensity factor of ($\Delta\sqrt{G}$)$_{max,c}$, $K_{max,c}$. Fracture toughness values, K_{IC}, are also displayed (Figure 5-20).

	$\Delta\sqrt{G}$ - decreasing			$\Delta\sqrt{G}$-increasing		Fracture tests
	$(\Delta\sqrt{G})_{th}$ (kJ/m^2)$^{1/2}$	A	n	$(\sqrt{G})_{max,c}$ (kJ/m^2)$^{1/2}$	$K_{max,c}$ (MPa-m$^{1/2}$)	K_{IC} (MPa-m$^{1/2}$)
SLS 0° orientation	1.3 ± 0.1	6-10^{-6}	9 ± 2	2.6 ± 0.2	3.7 ± 0.3	3.2 ± 0.2
SLS 90° orientation	1.1 ± 0.2	10-10^{-6}	10 ± 2	2.5 ± 0.3	3.6 ± 0.5	2.9 ± 0.2
IM	1.0 ± 0.2	5-10^{-6}	9.0 ± 0.5	3.0 ± 0.3	3.7 ± 0.4	3.1 ± 0.5

linear relationship between the crack growth rate and the control parameter described by the Paris law (or *eq. (2-2))* and region III, dependent on the fracture toughness K_{IC} as the crack growth rates approach instability. The reason is that these curves were achieved from constant load amplitude tests or $\Delta\sqrt{G}$-increasing tests.

The figures show the common scatter due to extrinsic factors like the experimental ones, such as material and geometry variability or variation in the testing conditions, and intrinsic factors as the probabilistic nature of the fatigue phenomenon itself [176]. For the characterization of region I and the determination of the control parameter threshold value, $(\Delta\sqrt{G})_{th}$, $\Delta\sqrt{G}$- decreasing tests were performed starting at a specific *AVG* level to guarantee some data overlap and consequently, to confirm the fatigue crack growth behaviour.

The experimental curves were fitted to equation *(2-2)* and the average values are shown in *Table 5-7*.

From the $\Delta\sqrt{G}$ -increasing tests, the maximum values of the control parameter of the last cycle before catastrophic failure, $\left(\sqrt{G}\right)_{max,c}$, their equivalent values *max,c* in term of the stress intensity factor, $K_{max,c}$, and the fracture toughness, K_{IC}, determined from fracture tests and contained in *Figure 5-20*, have been also included to facilitate the analysis. Furthermore, the threshold values of the crack driving force, $(\Delta\sqrt{G})_{th}$, obtained from $\Delta\sqrt{G}$ -decreasing tests are also displayed.

Moreover, to shed more light to the study, *Figure 5-30* gathers in one single diagram the fatigue crack propagation behaviour of *SLS* PA-12 at 0° and at 90° orientations and of *IM* PA-12. The characteristic dispersion of each material and condition has been represented with an envelope.

All this information reveals that the fatigue crack growth behaviour is very similar independently of orientation and manufacturing technique but there are some point differences worth mentioning. The effect of the load direction with regard to the layered structure of *SLS* PA-12 on the fatigue crack growth behaviour is obvious as *SLS* PA-12 at 0° orientation shows higher threshold values and smaller values of the exponent of the Paris law than those of *SLS* PA-12 at 90° orientation. Therefore, it can be concluded that the fatigue crack growth resistance is worse when the load is applied along the building direction, that is, at 90° orientation.

When analysing the influence of the manufacturing process, the threshold values of *IM* PA-12 are the smallest, but the steepness of the Paris law curve is similar to that of *SLS* PA-12 at 0° orientation. So, the fatigue crack growth behaviour of *IM* PA-12 is in between those of *SLS* PA-12 at 0° and at 90° orientations.

Figure 5-30. Fatigue crack growth behaviour comparison for PA-12 manufactured by SLS at 0" orientation (blue) and at 90°orientation (green) and by IM (red).

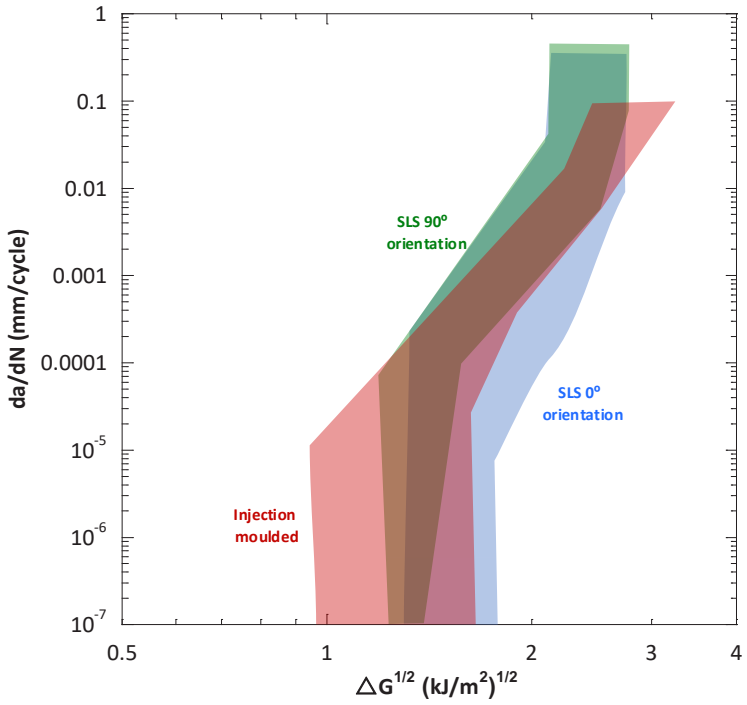

The region III of the fatigue crack growth life is characterized by the maximum value of the control parameter of the last cycle before rupture. Independently of the material or testing condition, the values were around 10% higher than the fracture toughness measured via standard fracture tests.

There is scarce literature regarding this topic in the literature. In principle, the exponents of the Paris law of *SLS* PA-12 are smaller than those obtained by Salazar et al. [39]. Nevertheless, it is worth mentioning that these authors employed *ΔK* as the crack driving force and the starting PA-12 powder and manufacturing machine were different to those used for the processing of the materials under study. Although Blattmeier et al. [124] analysed the influence of the load direction with respect to the layered structure in *SLS* PA-12, they observed no differences in the fatigue crack propagation of specimens tested at 0° and 90° orientations. And their curves are difficult to compare to those in the present work because firstly, the control parameter is ΔK and there are no fitting values to a Paris-law equation and secondly, those curves were not obtained under constant load amplitude tests. Finally, the only works focused on the fatigue crack propagation of *IM* PA-12 are those of Blattmeier et al.

[124] and Boukhili et al. [79]. The former obtained a fatigue crack growth behaviour of *IM* PA-12 clearly worse than that of *SLS* PA-12 and the latter realized that *ΔK* is not a valid crack driving force and also did not include the fitting values of the Paris-law equation.

5.7.1 Fractographic analysis from fatigue crack growth tests

The panoramic view of the fracture surfaces of *SLS* PA-12 at 0° and 90° orientations and of *IM* PA-12 are displayed in *Figure 5-31.a, Figure 5-31 .b* and *Figure 5-31 .c*, respectively. The arrow indicates the crack growth direction.

Firstly, the most characteristic feature of the fracture surfaces of *SLS* PA-12 is the high number of pores evenly distributed over the entire surface *(Figure 5-31.a, Figure 5-31 .b)*. According to Caulfield et al. [33], these pores are the result of the lack of powder particles melting during sintering, producing a poor fusion in the surrounding area. Another important feature is the discernible horizontal lines with an equidistant separation of 200 pm observed in the low magnification analysis of the fracture surfaces of *SLS* PA-12 at 0° orientation *(Figure 5-31.a)*. This distance matches with the manufacturing layer thickness (*Table 4.2*) so, the sintering among layers was defective as the fusion and sintering of one layer with the one underneath was not complete. Some authors have associated these lines with a low energy density supplied during the manufacturing process [33], [37].

Secondly, when comparing the 0° and 90° orientations, the fracture surfaces obtained at 90° orientation *(Figure 5-31.b*) was much smoother than that at 0° orientation *(Figure 5-31.a*). The crack tends to propagate along one single layer but when a coalescence of pores or defects occurs, this can lead to the jump of the crack to adjacent layers. This could explain the worse fatigue crack propagation at 90° orientation.

Thirdly, the panoramic view of the fracture surfaces of the *IM* PA-12 samples is completely smooth and plain, a striking contrast when compared to the morphology of *SLS* PA-12 *(Figure 5-31.c)*.

In order to identify the deformation and fracture mechanisms, *Figure 5-32.a , Figure 5-32.b* and *Figure 5-32.c* show detailed fracture surfaces of *SLS* PA-12 at 0° and 90° orientations and of *IM* PA-12, respectively. Independently of the manufacturing technique or the orientation, the mechanism of deformation and failure is the formation, growth and coalescence of crazes, followed by a fibrillation of the amorphous phase till final rupture.

This type of damage progression leaves as marks the patchwork pattern displayed in *Figure 5-33*, being the only difference, the size of the craters and

the more or less plastic deformation of the amorphous filaments surrounding them. In general, the stretched amorphous filaments are the most prominent in the *SLS* PA-12 at 0° orientation *(Figure 5-33.a*), less significant in the *SLS* PA-12 at 90° orientation *(Figure 5-33.b*) and not so remarkable in *IM* PA12 (*Figure 5-33.c*).

It is in these deformed amorphous filaments where fatigue striations were observed (*Figure 5-34*), being less numerous in the *IM* PA-12 *(Figure 5-34.c*) compared with SLS ones *(Figure 5-34.a* and *Figure 5-34.b*).

Therefore, the rough fracture surface (Figure 5-31.a, and Figure 5-32.a) together with the high deformed amorphous filaments in *SLS* PA-12 at 0°

Figure 5-31. Panoramic view of the fracture surfaces obtained from fatigue crack growth tests of PA-12 manufactured by (a) SLS at 0°orientation, (b) SLS at 90° orientation (b) and (c) IM. The arrow points out the crack growth direction.

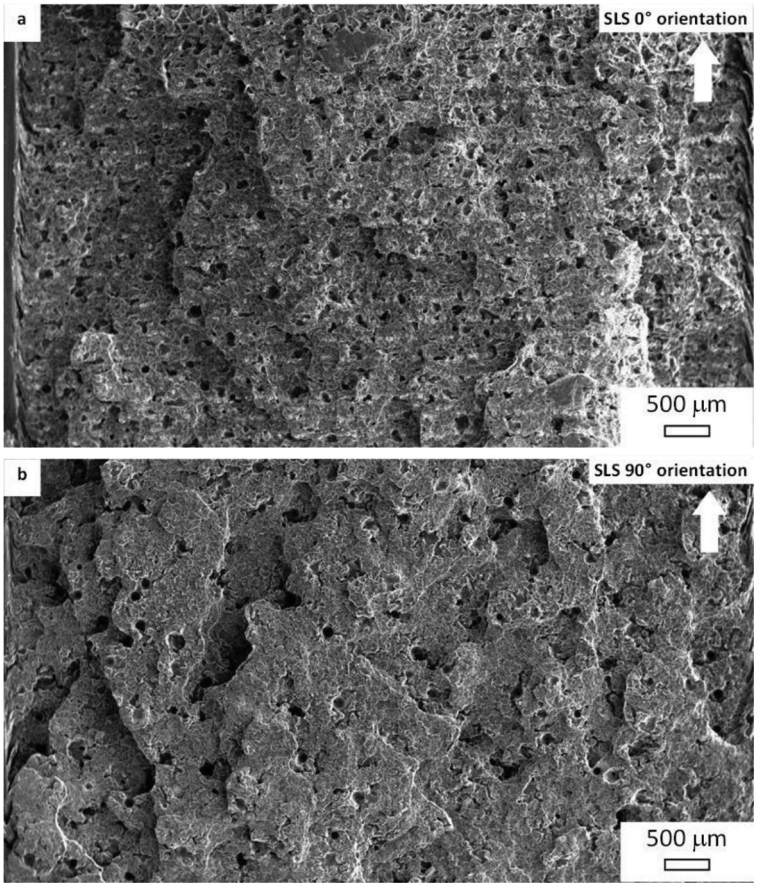

Figure 5-31. Panoramic view of the fracture surfaces obtained from fatigue crack growth tests of PA-12 manufactured by (a) SLS at 0°orientation, (b) SLS at 90° orientation (b) and (c) IM. The arrow points out the crack growth direction.

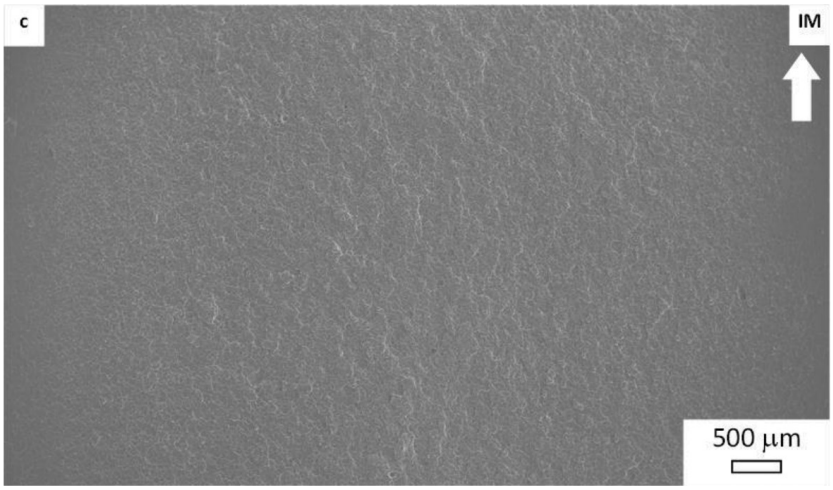

Figure 5-32. Detail cf the fracture surfaces obtained from fatigue crack growth tests of PA-12 manufactured by (a) SLS at 0°orientation, by (b) SLS at 90° orientation (b) and (c) by IM.

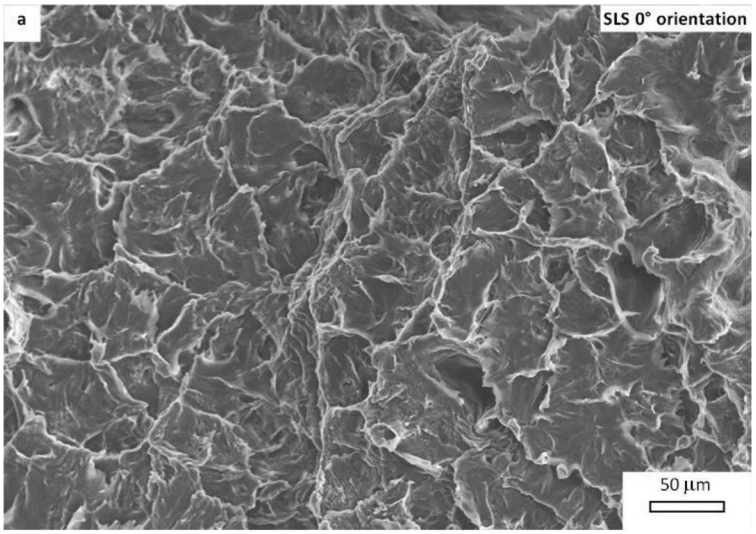

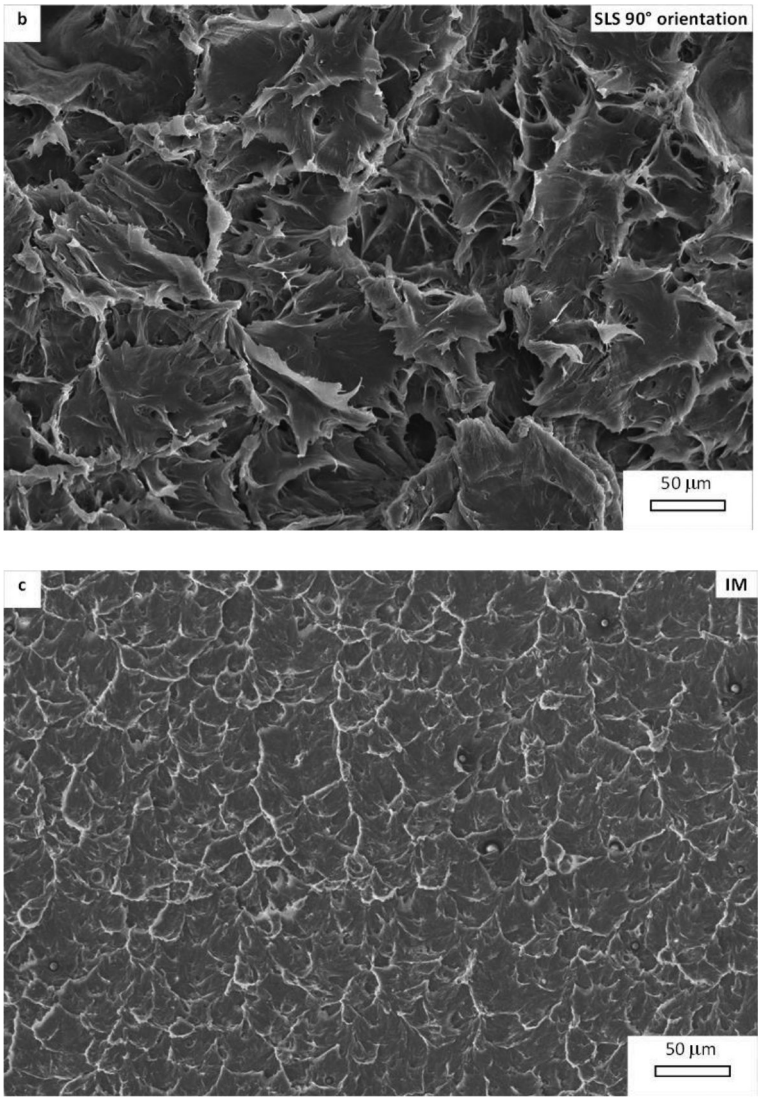

orientation (*Figure 5-34.a*) seems to be the reason of the best fatigue crack growth behaviour.

A more in-depth analysis of the nucleation and progression of the mechanism of failure during fatigue could be performed thanks to the fractographic analysis at high magnification shown in *Figure 5-35*.

Figure 5-33. Detail of the patchwork structure due to craze formation of PA-12 manufactured by SLS at 0° orientation (a) and at 90° orientation (b) and by IM (c). The nucleation sites of damage initiation are pointed out by arrows. The white arrows point to unmolten particles or the voids left behind by them and the blue arrows point to spherulitic nuclei.

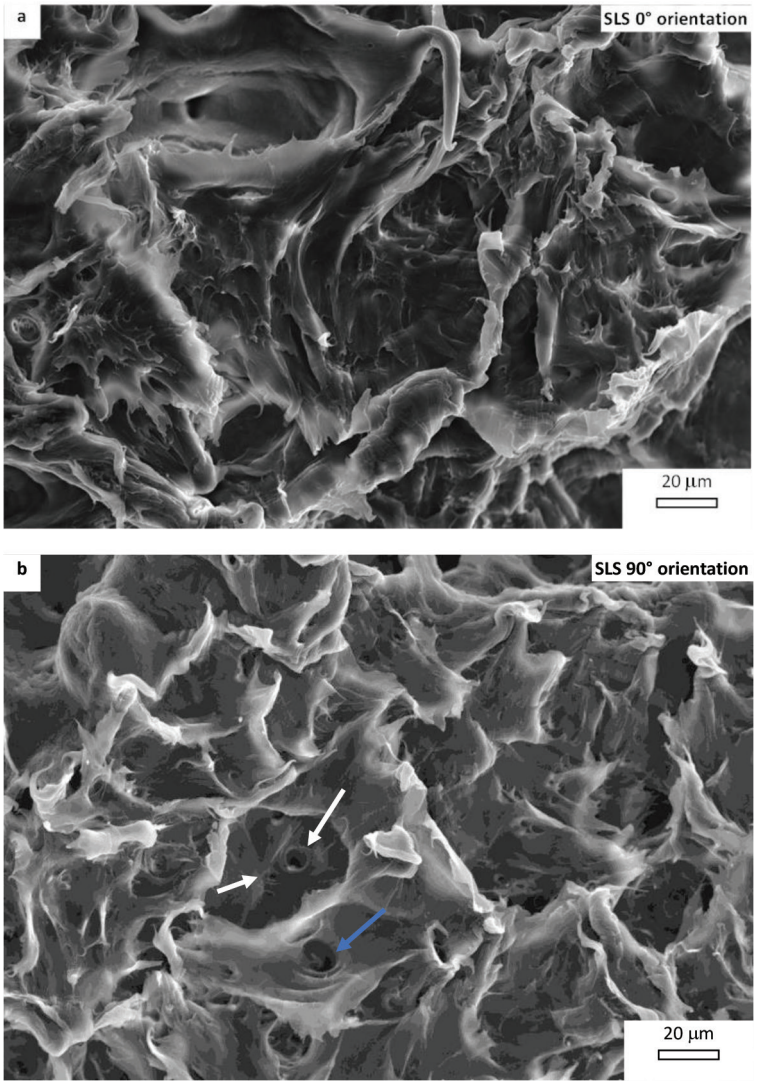

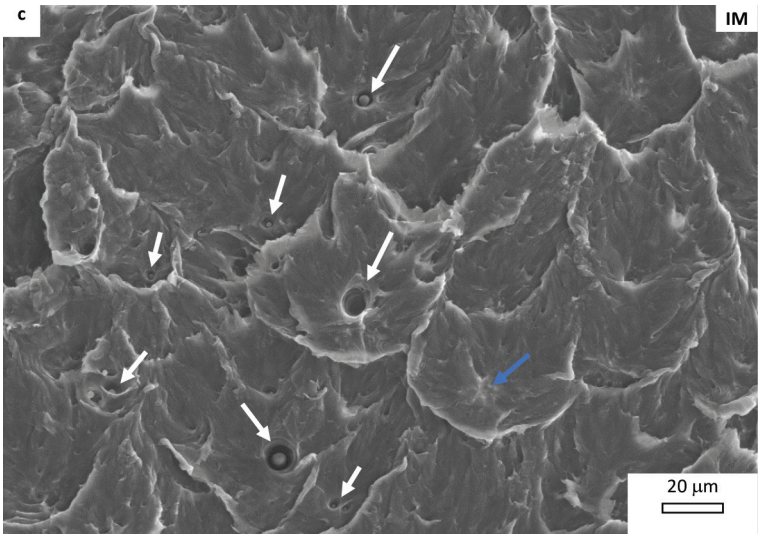

Figure 5-34. Fatigue river markings in amorphous filaments left behind the crack growth that surround the dimples generated after craze nucleation, growth and coalescence of (a) SLS PA-12 at 0 ° orientation, (b) SLS PA-12 at 90 ° orientation and of (c) IM PA-12.

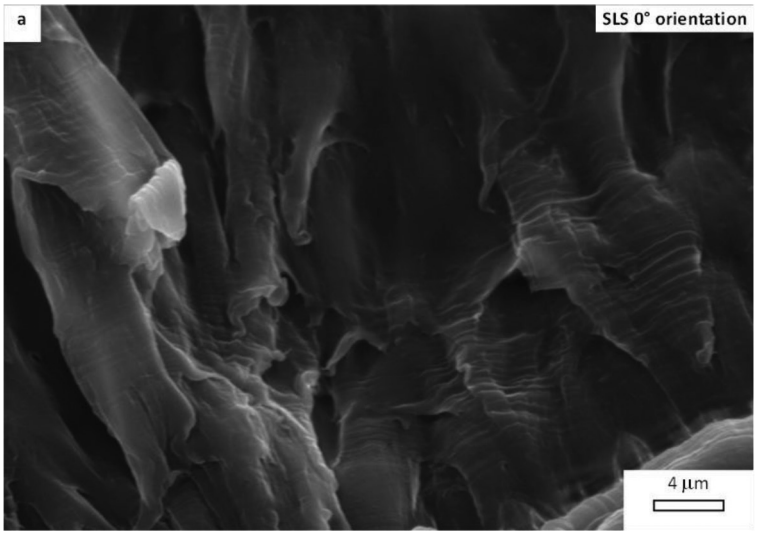

Figure 5-34. Fatigue river markings in amorphous filaments left behind the crack growth that surround the dimples generated after craze nucleation, growth and coalescence of (a) SLS PA-12 at 0 ° orientation, (b) SLS PA-12 at 90 ° orientation and of (c) IM PA-12. (Continued)

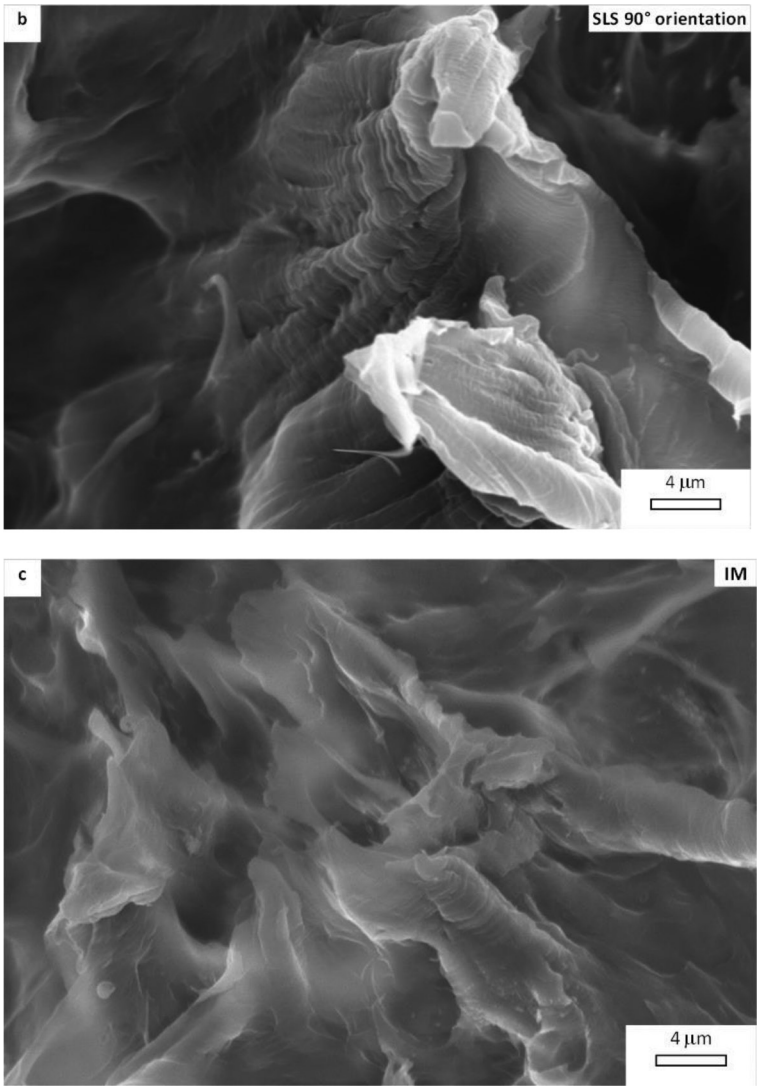

In this patchy surface, pores and in most cases, some unmolten particles at the centre of the craters are observed and shown with white arrows pointing at the particles in *Figure 5-33.b* and *Figure 5-33.c* for *SLS* at 90° orientation and for *IM* PA-12, respectively, and in *Figure 5-35*. These defects act as nucleation

Figure 5-35. Detail of the micromechanism of failure, where the craters left behind the fatigue crack path are originally generated by unmolten particles (pointed out by white arrows) or by spherulitic nuclei in form of ill-defined discs (a) or irregular rectangles (b), that act as damage precursors (pointed out by blue arrows).

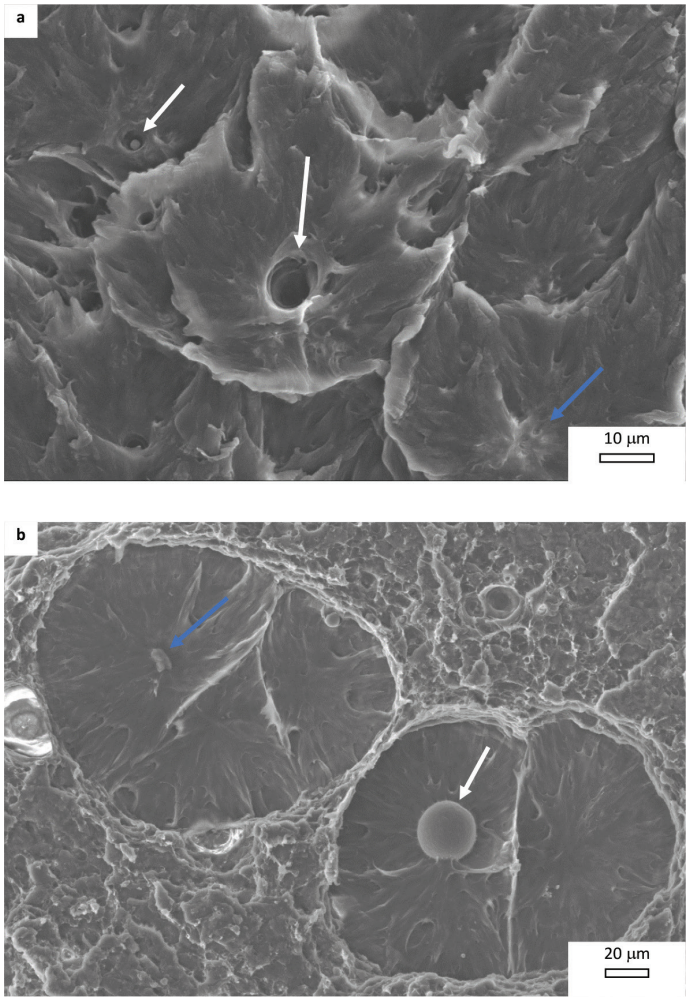

sites during the crazes formation being not the only responsible of the failure initiation. The crystalline structure plays an important role in the initiation damage during cycling loading as pointed out by several authors [162], [177], [178].

During fatigue, the high deformation occurring at the crack tip is the origin of void nucleation between the crystalline lamellae within the spherulite, oriented perpendicularly or at angle of approximately 45° to the applied load direction [177]. This leads to an intra-spherulitic or trans-spherulitic failure in the

equatorial plane, exposing in some occasions the nucleus of the spherulite, which has the appearance of an irregular rectangle (pointed out by a blue in *Figure 5-33.b and Figure 5-35.b*) or an ill-defined disc (pointed out by a blue arrow in *IM* PA-12 in *Figure 5-33.c and in Figure 5-35.a*).

Some authors have linked the dimensions of the patchwork patterns with the spherulite sizes. In this case, the crater size was around 50 pm for *SLS* PA-12 and 20-30 pm for *IM* PA-12 which is coincident with the spherulitic dimensions collected in *Table 5-3*. The bigger discrepancy was in *IM* PA-12. However, the fractographic analysis has shown that in *IM* PA-12, the damage was related with the spherulitic structure in a way that the micromechanism of failure is linked not only to individual spherulites but also to spherulite colonies when the former are extremely fine.

5.8 Fatigue life analysis

Figure 5-36. Lifetime fatigue curves of IM PA-12 and SLS PA-12 0 ° and 90 ° orientations. O→ symbol represents run-outs, that is, tests which reached 10^6 cycles without break.

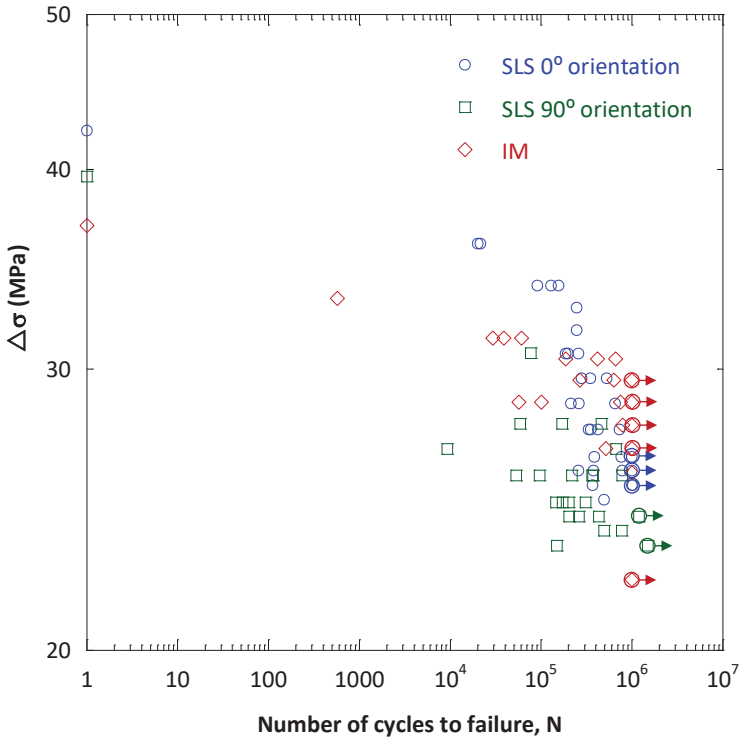

The results of the fatigue life tests carried out according to the ASTM D7791 standard recommendations are presented in the *Figure 5-36*. The tensile strength represented as the value at one cycle was also included, as well as the tests which reached 10^6 cycles without failure (run-outs). A first look at the graph evidences not big differences between either distinct orientations or manufacturing processes. Nevertheless, some dissimilarities are important to highlight.

SLS PA-12 at 0° orientation exhibited better fatigue life resistance than at 90° orientation despite the similarity in the porosity percentage (*Table 5-1*) and in the surface roughness values (*Table 5-2*). The weak interlayer strength seems to be behind this behaviour, as the defective sintering among layers as well as its physical discontinuity has been observed in the fractographic analysis *(Figure 5-31.a*).

Attending to the manufacturing process, *IM* PA-12 presented a mixed behaviour, that is, showed a better fatigue resistance than *SLS* PA-12 at both orientations near 10^6 cycles but a lower fatigue life resistance when the number of cycles to break was around 10^5. At those number of cycles, the behaviour of *SLS* PA-12 at 0° orientation is above that of *IM* PA-12.

In order to fit these results to the Basquin's equation, the average values of the number of cycles to failure for each load level were considered and represented in *Figure 5-37*. Attending to the values of the R^2 coefficient resulting from the fitting of the experimental values to the Basquin's law (*eq. (4-28)*), the scatter for all materials and conditions was in general very high, especially for *SLS* PA-12 at 90° orientation.

Table 5-8 gathers the Basquin coefficients of *SLS* PA-12 at 0° and 90° orientations and of *IM* PA-12. While the exponents of m_B of *SLS* at both orientations were similar, there is a big difference with that of the *IM* PA-12 which was one half.

For the determination of the fatigue limit at 10^6 cycles, *Figure 5-38.a, Figure 5-38.b* and *Figure 5-38.c* show the up-and-down fatigue test results of *SLS*

Table 5-8. Basquin constants from S-N curves of IM PA-12 and SLS PA-12 at 0 ° and at 90 ° orientations.

	B_B	m_B
SLS 0° orientation	111.1	-0.11
SLS 90° orientation	83.1	-0.09
IM	54.4	-0.05

Figure 5-37. Lifetime fatigue curves IM PA-12 and SLS PA-12 at 0 ° and at 90 ° orientations representing the average values of each load level. The fitting of the experimental results to the Basquin type equation $\Delta\sigma = B_B N^{m_B}$ is also displayed.

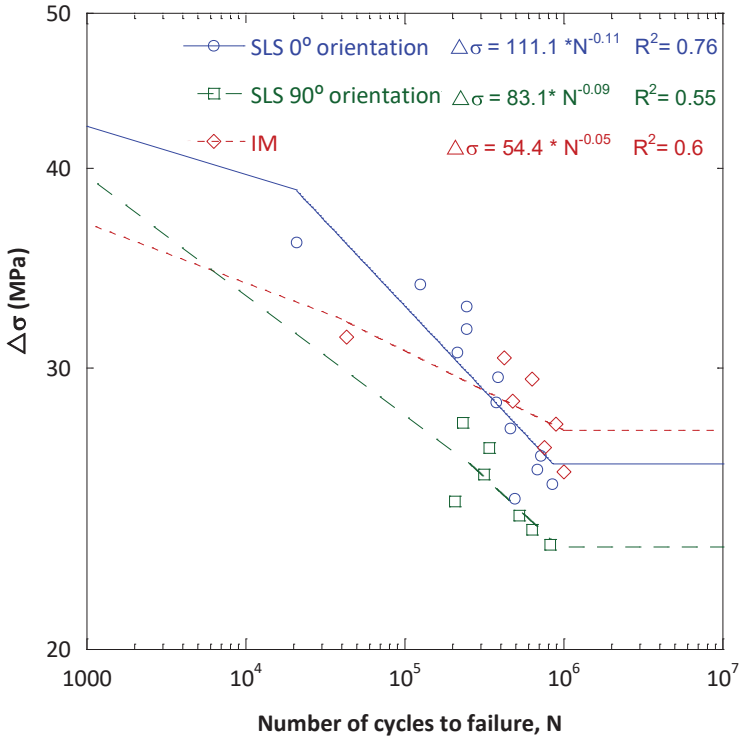

PA- 12 at 0° orientation, *SLS* PA-12 at 90° orientation and *IM* PA-12, respectively. These graphs represent the run-out tests with a green circle and the failure tests with a red cross. In order to obtain more accurate results, in case of *SLS* PA-12 at 0° orientation, after 6 tests, the initial stress step between run-out and failure was reduced to one half of the initial value, followed by a second reduction of a 2.5 % of the initial value, analysing a total of 5 stress amplitudes. For *SLS* PA-12 at 90° orientation, only a first reduction of the step from $2.5\%\sigma_T$ to $1.25\%\sigma_T$ was implemented, with a total of 4 stress amplitudes. In case of *IM* PA-12, two step reductions were carried out, beginning with the first one of $11.5\%\sigma_T$ and followed by a second one of $2.5\%\sigma_T$. The total number of stress amplitudes examined were 6.

Table 5-9 displays the fatigue lifetime results used in the estimation of the fatigue limit at 10^6 cycles for both orientations of *SLS* PA-12 and of *IM* PA-12.

Figure 5-38. Up-and-down fatigue tests for the estimation of the fatigue limit at 10^6 cycles: (a) SLS PA-12 at 0° orientation, (b) SLS PA-12 at 90°orientation and (c) IM PA-12. The representations include run-out tests O and failure ones X.

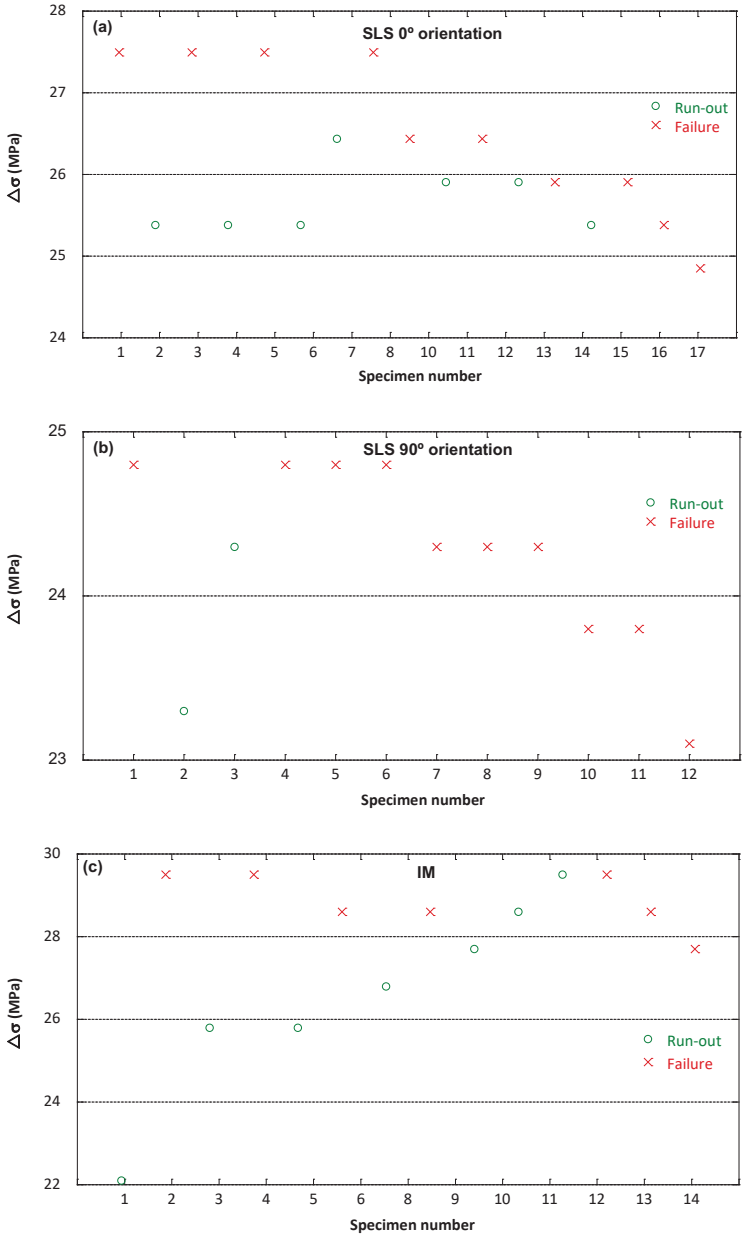

Table 5-9. Results cf the fatigue ifetime test for the determination cf the fatigue limit at 10^6 cycles, $\Delta\sigma_{fl}$, cf SLS PA-12 at 0° and 90° orientations and of IM PA-12, including the stress amplitude, $\Delta\sigma$, number of failure tests, f_i, and of run-outs, r_i.

Manufacturing orientation	$\Delta\sigma_i$ (MPa)	Number of failure tests, f_i	Number of Runout tests, r_i	$\Delta\sigma_{fl}$ (MPa)
0°	24.8	1	0	26 ± 1
	25.4	1	3	
	25.9	3	2	
	26.5	2	1	
	27.5	4	0	
		$\sum f$=11	$\sum r$=6	
		n = 17		
90°	23.3	1	1	23 ± 1
	23.8	2	0	
	24.3	3	1	
	24.8	4	0	
		$\sum f$=10	$\sum r$=2	
		n = 12		
IM	22.1	0	1	28 ± 1
	25.8	0	2	
	26.8	0		
	27.7	1	1	
	28.6	3	1	
IM	29.5	3	1	
		$\sum f$=7	$\sum r$=7	
		n = 14		

It shows the number of failure tests, the number of "Run-outs" tests for each stress level, $\Delta\sigma_i$, and the fatigue limit at 10^6 Cycles, $\Delta\sigma_{fl}$, resulting from the application of the maximum likelihood method assuming a normal distribution, as described in the previous chapter.

SLS PA-12 at 0° orientation had a statistical fatigue limit at 10^6 cycles 13% higher than the one at 90° orientation. However, *IM* PA-12 had the highest fatigue limit, being 8% higher than the one of *SLS* PA-12 at 0° orientation.

5.8.1 Fractographic analysis of fatigue life tests

A panoramic view of the fracture surfaces of *SLS* PA-12 at 0° and 90° orientations and of *IM* PA-12 are shown in *Figure 5-39.a, Figure 5-39.b* and *Figure 5-39.c*, respectively. The white arrow indicates the crack growth direction on each specimen and, in all cases, the cracks propagated from the left side of the images to the right. It is obvious the influence of the manufacturing technique on the fractographic analysis of the broken specimens tested for the stress life fatigue curves characterization. While the fracture surfaces of *SLS* PA-12 maintained the initial cross-sectional dimensions, all the *IM* PA-12 fracture surfaces undergone a strong reduction of the initial cross section area despite the testing conditions were under High Cycle regime.

Moreover, while in all *SLS* PA-12 fracture surfaces three different areas were distinguishable and outlined by three different colours over the surfaces, in *IM* PA-12, only two zones were discernible. For all the cases, the zone delimited by the dashed green line is the subcritical crack growth area, which

Figure 5-39. Panoramic views of (a) SLS PA-12 at 0° orientation (a) SLS PA-12 at 90° orientation and (c) IM PA-12, identifying different: Region I or subcritical crack growth zone outlined with a dashed green line, Region II or transition region delineated with a dotted blue line and region III or unstable crack growth region surrounded with a dotted red line.

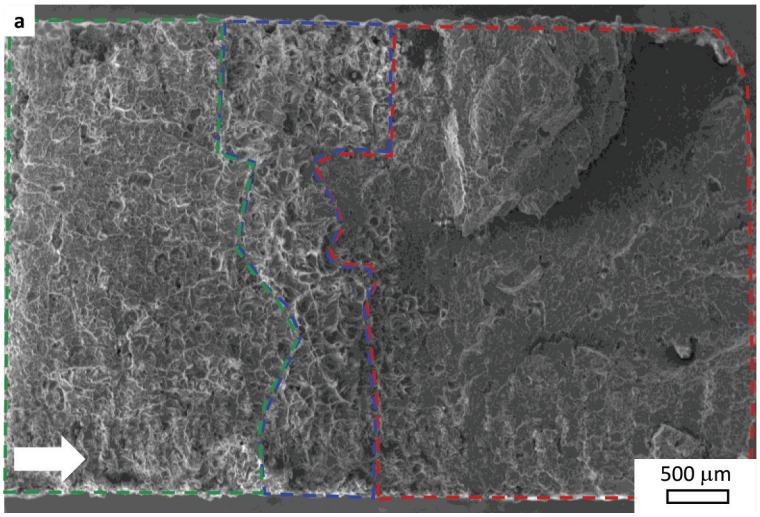

Figure 5-39. Panoramic views of (a) SLS PA-12 at 0° orientation (a) SLS PA-12 at 90° orientation and (c) IM PA-12, identifying different: Region I or subcritical crack growth zone outlined with a dashed green line, Region II or transition region delineated with a dotted blue line and region III or unstable crack growth region surrounded with a dotted red line. (Continued)

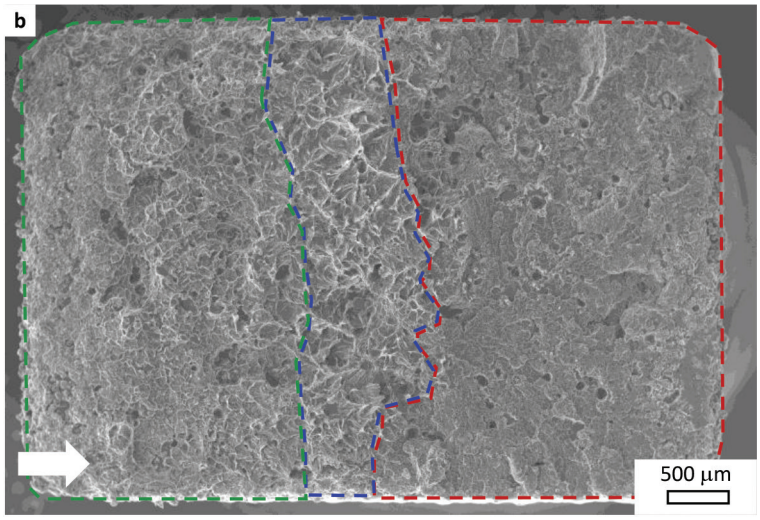

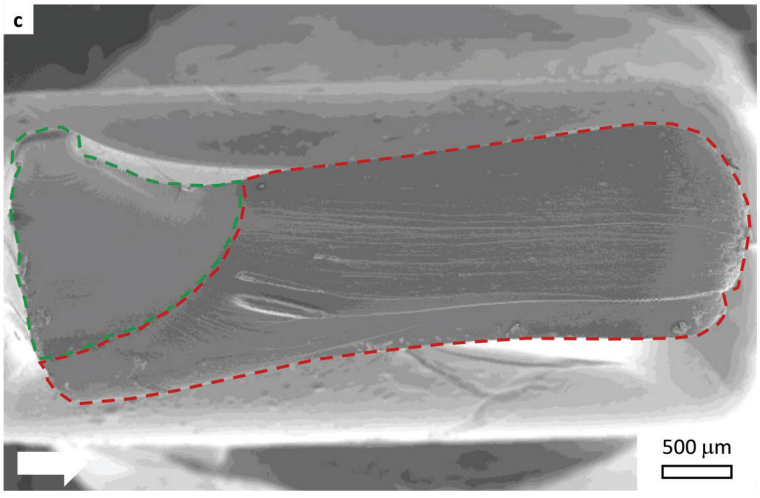

is followed by a transition region outlined in dashed blue line (only observed in *SLS* PA-12), and finally, the unstable crack growth region delineated in dashed red line.

For *SLS* PA-12, the subcritical area was characterized by a patchy irregular surface, unequivocal morphological sign of nucleation, growth and coalescence of crazes in both the early stages of formation of the macroscopic crack and subsequent propagation. The crater size of the marks left by this damage advancement was of around 50 µm, which matches with the spherulitic size determined in section *5.3* (*Figure 5-40*). This fact revealed a hampered crack growth due to the presence of spherulites in a trans-spherulitic growth mode. Therefore, the crack was nucleated at some point of the surface, favoured by the high roughness (*Table 5-2*), and once generated progressed through the spherulites and in many cases, going through their equatorial plane. This mechanism of failure was also observed in the fracture surfaces of *SLS* PA-12 obtained from tensile tests (*section 5.5.1)*, from fracture toughness tests (*section 5.6.1)* and from fatigue crack growth tests (*section 5.7)*.

The only difference between 0° and 90° orientations in *SLS* PA-12 was that this area seemed to be rougher in the samples tested at 0° orientation that in those tested at 90° orientation.

In case of *IM* PA-12, the crack also nucleated at some point at the surface, belonging to the skin layer due to the presence of small sink marks *(Figure 5-39.c*). The morphology of the subcritical crack growth area is completely different to that observed in *SLS* PA-12, characterized by fatigue striations bowed out in the direction of the crack propagation (*Figure 5-41*). The fatigue striations spacing became larger as moving away from the surface defect responsible of the crack nucleation.

Figure 5-40. Morphology of the subcritical crack growth zone of SLS PA-12.

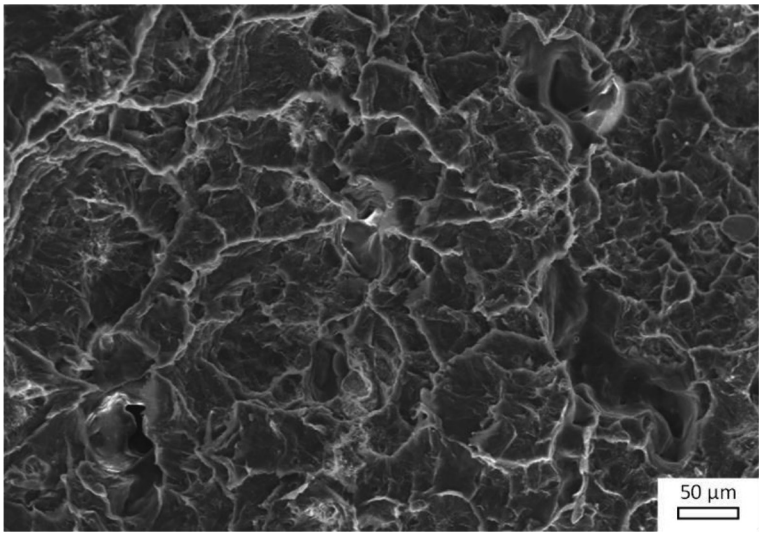

Figure 5-41. Morphology of the subcritical crack growth zone of IM PA-12.

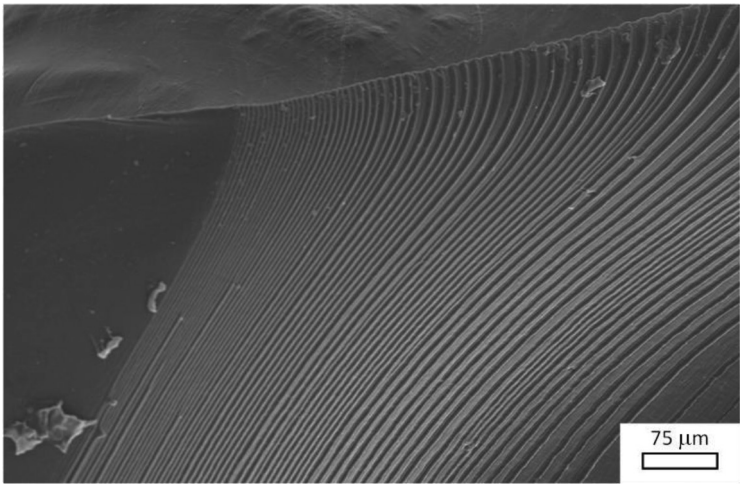

Figure 5-42. Transition region: the filaments of amorphous PA-12 suffered high elongation along crack propagation direction.

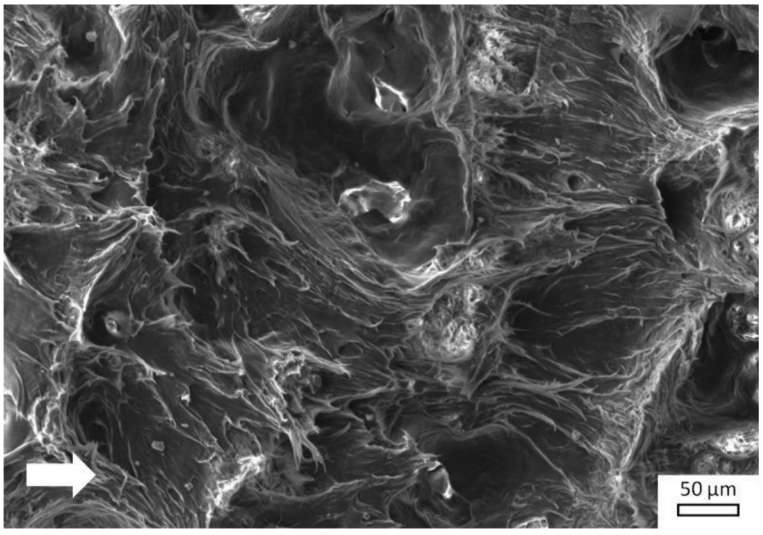

In *SLS* PA-12, following the subcritical crack growth zone, a transition region, was observed and outlined in dashed blue line in *Figure 5-39.a* and *Figure 5-39.b*, and shown in detail in *Figure 5-42*. This region was characterised by a high ductile tearing of amorphous filaments around dimples, which in some

Figure 5-43. Fatigue marks visible in the high elongated filaments in the transition region.

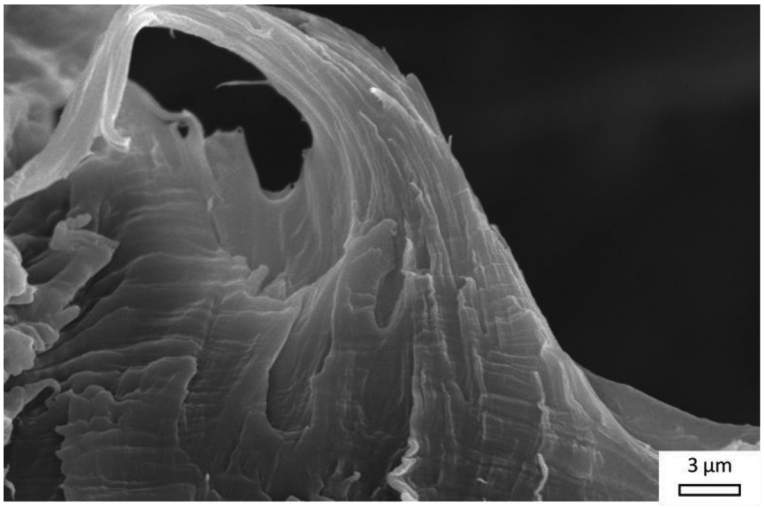

cases could be hidden by the plastic deformation. The amorphous filaments were aligned along the crack propagation direction and fatigue striations were only observed on them *(Figure 5-43)*. No differences were appreciated between *SLS* PA-12 at 0° and at 90° orientations. Moreover, the transition region was not observed in none of the fracture surfaces of *IM* PA-12.

In *SLS* PA-12, following the transition region, the unstable crack growth region, outlined in dotted red line in *Figure 5-39.a* and *Figure 5-39.b* was found. The border between these two regions was continuous *(Figure 5-44.a*) and the morphology was plain, with an irregular pattern and with no trace of distinguishable elongation of amorphous material *(Figure 5-44.b*). No differences in this zone were discernible between both orientations in *SLS* PA-12.

Finally, *Figure 5-45* shows a detail of the unstable crack growth zone of *IM* PA- 12 outlined in dotted red line in *Figure 5-39.c*. The surface was smooth and plain with no characteristic feature except for some very fine river markings along the crack growth direction.

5.8.2 Application of the Fracture Mechanics approach to the fatigue life tests

The fractographic analysis of the broken specimens revealed a scheme of the damage progression till catastrophic failure occurring during the fatigue life tests. The nucleation of the crack occurred at some point at the surface,

Figure 5-44. (a) Border between the transition zone and the unstable crack growth region, and (b) morphology of the unstable crack growth area of SLS PA-12.

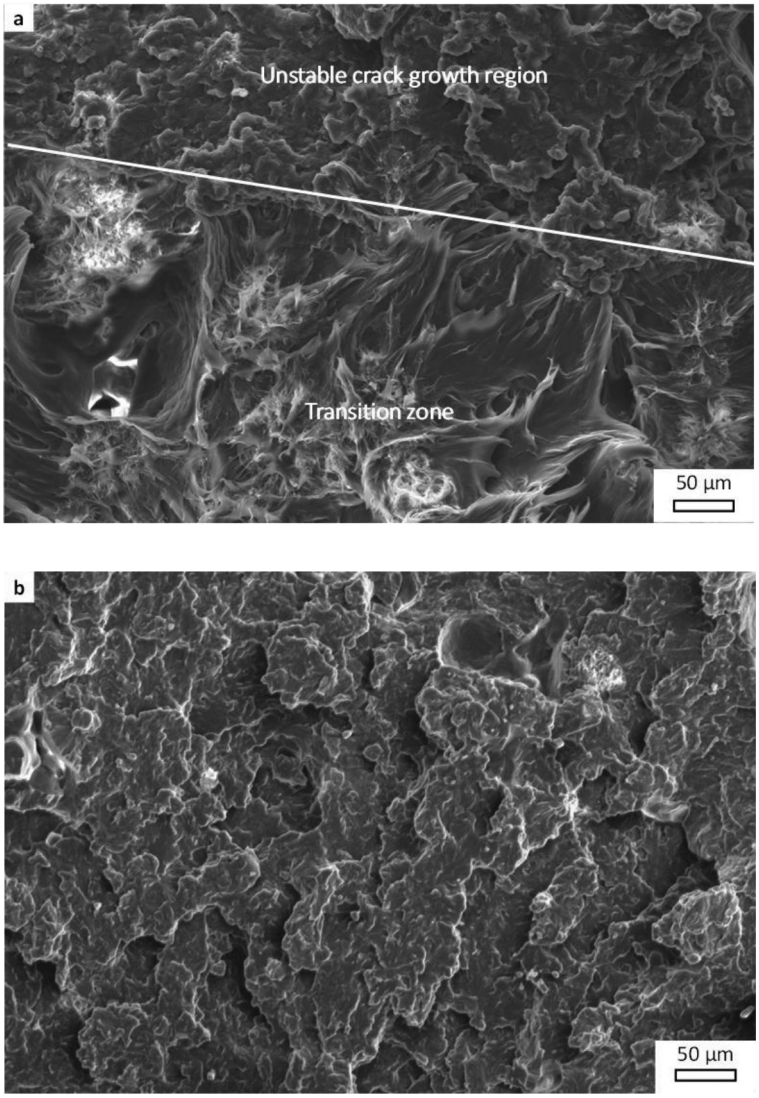

as a consequence of the high roughness in *SLS* PA-12 specimens or of the amorphous skin layer in *IM* PA-12 samples. The crack propagation occurred till reaching a critical value, coincident with the extension of the subcritical crack growth zone, a. At that moment, brittle failure occurred at the remnant ligament, giving rise a plastic deformation zone at the crack tip (transition region) followed by an undamaged polyamide (unstable crack growth zone) in

Figure 5-45. Morphology cf the unstable crack growth region cf IM PA-12.

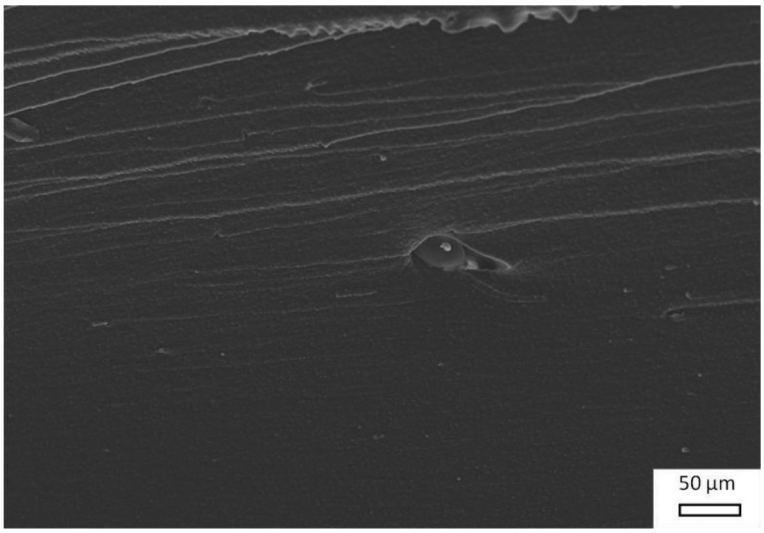

SLS PA-12. However, in *IM* PA-12, only unstable crack growth area was observable but with evident plastic deformation along the gage length of the sample due to a pronounced reduction of the initial cross-sectional area. Just because the non-negligible plastic deformation along the gage length in *IM* PA- 12, damage modelling using the Fracture Mechanics approach was only applied to *SLS* PA-12 at 0° and 90° orientations.

From the sketch of the different zones delineated in *Figure 5-39.a* and *Figure 5-39.b*, the fatigue life specimens with the subcritical crack growth area could be fitted in with SENT configuration at the instant of failure. So, the results obtained from the application of the Fracture Mechanics approach using data from the last cycle are shown in *Table 5-10* and *Table 5-11* for *SLS* PA-12 at 0° and 90° orientations, respectively.

From the analysis of the results, several points are remarkable and worth discussing. Firstly, a common trend can be observed for both orientations, the length of the subcritical crack growth is lower as the applied stress level increases. Secondly, the estimated energy at crack growth initiation values are in accordance with those achieved in standardized fracture tests shown in *section 5.6* for both orientations. Nevertheless, some deviations were obtained in *SLS* PA-12 at 0° orientation for the high stress levels of 0.8 and 0.85. For these testing conditions, the estimated values of *Jc* were extremely high and were not included in the computation of the average value displayed in bold in *Table 5-10*. To ascertain the possible reason of these overestimated

*Table 5-10. Estimation of the fracture toughness cf SLS PA-12 at 0°orientation from fatigue life tests damage modelling including the stress ration, $\frac{\sigma_{max}}{\sigma_T}$, the length of subcritical crack growth, a, the estimated value of the energy at growth initiation, J_c. *The average value in bold was calculated without the results at stress levels of 0.8 and 0.85.*

$\frac{\sigma_{max}}{\sigma_T}$	a (mm)	J_c (kJ/m²)
0.58	2.41	6.65
0.60	1.87	8.08
0.61	2.0 ± 0.2	6.7 ± 0.4
0.63	1.66	6.11
0.65	1.8 ± 0.1	6.9 ± 0.9
0.68	1.7 ± 0.1	6.8 ± 0.1
0.7	1.7 ± 0.1	7.3 ± 0.6
0.73	1.55	7.24
0.75	1.81	8.09
0.78	1.55	9.19
0.8	1.4 ± 0.1	10.2 ± 0.2
0.85	0.9 ± 0.1	12 ± 1
		7.1 ± 0.8*

Table 5-11. Estimation of the fracture toughness of SLS PA-12 at 90°orientation from fatigue life tests damage modelling including the stress ration, $\frac{\sigma_{max}}{\sigma_T}$, the length of subcritical crack growth, a, the estimated value of the energy at growth initiation, J_c.

$\frac{\sigma_{max}}{\sigma_T}$	a (mm)	J_c (kJ/m²)
0.60	2.0	6.47
0.65	1.9 ± 0.2	5.5 ± 0.4
0.7	1.82	6.79
0.78	1.56	7.53
		6.0 ± 0.8

Figure 5-46. Hysteresis loops obtained from the cyclic load-displacement records cf the last cycle before rupture of the tests at stress ratios of 0.7 and 0.85 performed in PA-12 at 0° orientation.

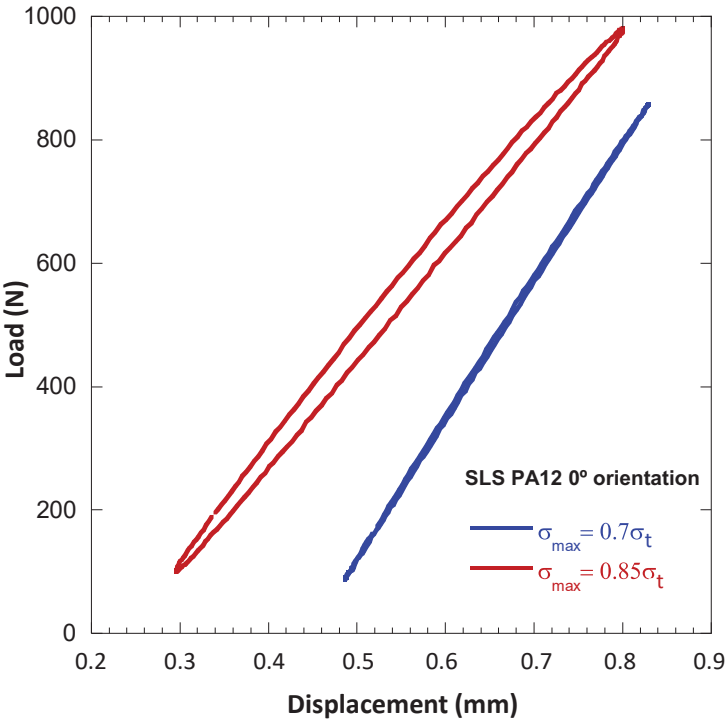

values of *Jc* at those stress levels, the hysteresis loops of the last cycle before failure were examined. *Figure 5-46* shows the hysteresis loops of the last cycle before failure of the fatigue life tests carried out at stress ratios of 0.7 and 0.85 of *SLS* PA-12 at 0° orientation. The main difference is that, while for the stress ratio of 0.7, the loading and unloading parts of the cyclic load-displacement record overlap, for the stress ratio of 0.85 an area within the loop is noticeable. This area represents dissipative energy per unit of volume due to viscoelasticity and/or plasticity, which can be the reason of the overestimation of the fracture parameters.

Another method to check the validity of the results is to determine the crack length from the unloading part of the load-displacement record of the last cycle using the following expression for SENT configuration [179]:

$$\frac{a}{W} = 2.072 - 16.411U + 29.6U^2 - 211.67U^3 + 236.857U^4 + 27.371U^5 - 179.74U^6 - 86.28U^7 + 171.764U^8$$

with U the normalized compliance obtained from the unloading part of the cyclic load-displacement record using equation (4-24). The calculations yield results which differed from the measured lengths of the subcritical crack growth zone in *Table 5-10* utmost 20% for stress level lower than 0.8 and more than 90% for stress level higher than 0.80.